

1
2
3
4
5 WEATHERING INTENSITY AND LITHIUM ISOTOPES:
6 A REACTIVE TRANSPORT PERSPECTIVE
7

8 Matthew J. Winnick^{1*}, Jennifer L. Druhan², Kate Maher³
9

10
11
12
13
14
15
16 ¹ Department of Geosciences
17 University of Massachusetts Amherst
18 Amherst, MA 01003, USA
19

20 ² Department of Geology
21 University of Illinois Urbana Champaign,
22 Urbana, IL
23

24 ³ Department of Earth System Science
25 Stanford University
26 Stanford, CA 94305, USA
27

28
29
30 * Corresponding Author:
31 mwinnick@umass.edu
32 627 N Pleasant St,
33 Morrill II Rm 233, Geosciences
34 Amherst, MA 01003, USA
35

36 This manuscript has undergone peer review and has been accepted in this form for publication
37 at the American Journal of Science. The final version of this manuscript, subject to proof-stage
38 changes will be available via the DOI link on the right-hand side of this webpage when
39 available. Please contact the authors with any feedback.

40 **ABSTRACT.** Lithium isotopes have emerged as a powerful tool to probe the response of
41 global weathering to changes in climate. Due to the preferential incorporation of ^6Li into
42 clay minerals during chemical weathering, the isotope ratio $\delta^7\text{Li}$ may be used to interrogate
43 the balance of primary mineral dissolution and clay precipitation. This balance has been
44 linked to relative rates of chemical and physical denudation, such that dissolved $\delta^7\text{Li}$
45 ($\delta^7\text{Li}_{\text{diss}}$) is highest at moderate weathering intensities when chemical and physical
46 denudation are comparable. However, we argue that current theory linking $\delta^7\text{Li}$ to
47 weathering regimes through fluid travel times are unable to explain observations of low
48 $\delta^7\text{Li}$ and high Li concentrations in rapidly eroding settings. In this study, we re-examine
49 the relationships between $\delta^7\text{Li}$, Li concentration, and weathering regime by incorporating
50 Li isotopes into simulations of weathering profiles using a reactive transport model
51 (CrunchFlow) that includes advective fluxes of regolith to simulate variable erosion rates in
52 response to uplift. In these simulations, fractionation is implemented through a kinetic
53 fractionation factor during clay precipitation, which allows the $\delta^7\text{Li}$ of dissolved and
54 suspended loads in the model to vary as a function of Li/Al ratios in primary and
55 secondary minerals. When the model is run over a range of infiltration and erosion rates,
56 simulations reproduce observed global patterns of $\delta^7\text{Li}_{\text{diss}}$ and suspended load $\delta^7\text{Li}$ as a
57 function of weathering intensity, controlled primarily by water travel times and mineral
58 residence times in weathered bedrock. We find that reduced water travel times at low
59 weathering intensity, however, are inconsistent with observations of high Li concentrations.
60 As an alternative, we demonstrate how the rapid weathering of soluble, Li-rich minerals
61 such as chlorite under low weathering intensities may resolve this apparent discrepancy
62 between data and theory. We also suggest that observed patterns are consistent with
63 geothermal Li sources under low weathering intensities. This work offers a foundation
64 guiding future studies in testing potential mechanisms underlying global riverine $\delta^7\text{Li}_{\text{diss}}$.

65
66 Key Words: Lithium isotopes, weathering regime, reactive transport model, chemical
67 weathering, critical zone isotopes

69 INTRODUCTION

70

71 Chemical weathering, comprising the dissolution of carbonate and silicate minerals along
72 with the oxidation of sulfides and petrogenic carbon, is thought to be a primary regulator of
73 atmospheric composition on geologic timescales. The connections between chemical weathering
74 and climate are therefore central to our understanding of the evolution of global biogeochemical
75 cycles through Earth history. Over the past two decades, lithium isotopes have emerged as a
76 powerful tool for characterizing the relationships between silicate weathering and past climates.
77 Proxy records of oceanic $\delta^7\text{Li}$ have been used, for example, to characterize connections between
78 weathering and Cenozoic cooling (Misra and Froelich, 2012; Li and West, 2014; Caves-
79 Rugenstien and others, 2019; Pogge von Strandmann and others, 2020), along with the response
80 of weathering to major carbon cycle perturbations including Ocean Anoxic Events (OAE's) 1
81 and 2 (Pogge von Strandmann and others, 2013; Lechler and others, 2015), the Permian-Triassic
82 boundary (Sun and others, 2018), and global glaciation events (Pogge von Strandmann and
83 others, 2017). Interpretations of these proxy records rely on modern observations of lithium
84 isotopes in weathering environments; however, even present-day connections between $\delta^7\text{Li}$ and
85 weathering dynamics have proven highly complex.

86 The use of lithium isotopes to probe weathering dynamics is enabled by the fact that the
87 lighter isotope, ^6Li , is preferentially incorporated into secondary minerals relative to the heavy
88 isotope, ^7Li , during the chemical weathering of primary minerals in bedrock. Here, $\delta^7\text{Li}$ is
89 defined in standard delta-notation as,

90

$$91 \quad \delta^7\text{Li} = \left(\frac{{}^7\text{Li}/{}^6\text{Li}_{\text{sample}}}{{}^7\text{Li}/{}^6\text{Li}_{\text{L-SVEC}}} - 1 \right) * 1000\text{‰} \quad (1),$$

92

93 where $({}^7\text{Li}/{}^6\text{Li})_{\text{L-SVEC}}$ is the isotope ratio of the L-SVEC standard, 12.2998 (Flesch and others,
94 1973).

95 Isotope fractionation during secondary mineral precipitation represents a combination of
96 effects relating to the incorporation of Li into mineral structural sites (Williams and Hervig,
97 2005; Vigier and others, 2008; Wimpenny and others, 2010) and inner-sphere sorption (Zhang
98 and others, 1998; Anghel and others, 2002; Pistiner and Henderson, 2003; Hindshaw and others,
99 2019) as potentially modified by OH group abundance (Millot and Girard, 2007). Secondary
100 mineral phase $\delta^7\text{Li}$ values are thus offset from primary minerals by -5‰ to -30‰, reflecting this
101 preferential uptake of ^6Li (Vigier and others, 2008; Chan and others, 1992; Williams and Hervig,

102 2005). As a result, global riverine $\delta^7\text{Li}_{\text{diss}}$ values (-2‰→30‰) are significantly enriched relative
103 to average upper continental crust materials (-2‰–6‰) (Tomascak, 2004; Pogge von
104 Strandmann and others, 2020).

105 When solutes are enriched in ^7Li relative to bedrock, the dissolved $\delta^7\text{Li}$ ($\delta^7\text{Li}_{\text{diss}}$) reflects
106 the balance between Li release from primary mineral dissolution and Li incorporation into
107 secondary minerals. During congruent weathering, the Li released from primary minerals
108 remains in solution and $\delta^7\text{Li}_{\text{diss}}$ resembles bedrock values; when weathering is incongruent and a
109 significant amount of Li is incorporated into secondary minerals, $\delta^7\text{Li}_{\text{diss}}$ is elevated relative to
110 the minerals. Accordingly, observations of modern river systems show that $\delta^7\text{Li}_{\text{diss}}$ varies as a
111 function of weathering congruency, or the fraction of Li released from primary mineral
112 dissolution that remains in solution and is not incorporated into secondary minerals (f_{Li})
113 (Dellinger and others, 2015). Notably, the overall pattern of this relationship segregates into two
114 unique relationships, one in upland environments where the degree of $\delta^7\text{Li}_{\text{diss}}$ elevation above
115 bedrock values varies as a linear function f_{Li} , and the second in floodplain environments where
116 $\delta^7\text{Li}_{\text{diss}}$ varies as a power-law or Rayleigh-style function of f_{Li} potentially due to scavenging of Li
117 by extant phases (Dellinger and others, 2015; Maffre and others, 2020) or the formation of
118 authigenic clays (Zhang and others, 2021). Here, we focus on Li fractionation processes
119 characteristic of upland regolith development.

120 Extending the relationship between $\delta^7\text{Li}$ and weathering congruence to a metric for
121 weathering fluxes has proven more difficult. For example, $\delta^7\text{Li}_{\text{diss}}$ has been empirically linked to
122 both chemical weathering fluxes and riverine Li concentrations within specific regions; however,
123 these relationships may be contradictory in both sign and magnitude when compared across
124 regions (Huh and others, 2001; Vigier and others, 2009; Millot and others, 2010). More recent
125 work, both theoretical and observational (Bouchez and others, 2013; Dellinger and others, 2015,
126 2017), has contended that $\delta^7\text{Li}_{\text{diss}}$ reflects weathering intensity (WI), or the ratio of chemical
127 weathering (W) to total denudation, D ($\sim E + W$). At steady state regolith thickness, regolith
128 production (RP) must equal total denudation (RP = E + W), hence we define WI = W/RP, as
129 outlined in figure 1. Within this framework, weathering congruence and subsequent $\delta^7\text{Li}_{\text{diss}}$ are
130 controlled by weathering intensity, which in turn dictates the combination of mineral residence-
131 and fluid travel times in the regolith.

132 In figure 1, Point A represents a condition of moderate WI where physical and chemical
133 erosion are comparable. Under these conditions, regolith profiles reflect the balance between
134 regolith production and denudation rates, as minerals are supplied via uplift and are partially
135 depleted towards the surface through chemical denudation before they are eroded. As a result of
136 these well-developed regolith profiles, fluid travel times during infiltration are sufficient to
137 support secondary mineral precipitation, mineral residence times are sufficient to support
138 secondary mineral accumulation, and weathering occurs incongruently. This situation results in
139 maximum $\delta^7\text{Li}_{\text{diss}}$ values and moderate Li concentrations ($[\text{Li}^+]$; $\sim 10^2$ nM; Dellinger and others,
140 2015). When chemical denudation rates are much greater than erosion or regolith production
141 (high WI, Point B), chemical weathering depletes primary minerals from soils (that is, supply-
142 limited weathering), and dissolved solutes represent the dissolution of low-solubility secondary
143 mineral phases, characteristic of wet tropical environments (von Blanckenburg and others, 2004).
144 Due to this low solubility and the preferential uptake of ^6Li during initial clay precipitation, clay
145 dissolution results in both low $[\text{Li}^+]$ (< 10 nM) and low $\delta^7\text{Li}_{\text{diss}}$.

146 Finally, under low WI conditions when physical erosion greatly outpaces chemical
147 weathering (Point C), mineral residence times in regolith are short such that secondary minerals
148 are unable to accumulate in significant amounts (that is, kinetic-limited weathering). Steady-state
149 weathering models that describe this behavior predict that under low WI, clay precipitation rates
150 are reduced relative to primary mineral dissolution rates (Chamberlain and others, 2005; Ferrier
151 and Kirchner, 2008), resulting in congruent weathering and low, bedrock-like $\delta^7\text{Li}_{\text{diss}}$ values
152 (Bouchez and others, 2013). This conceptual model of congruent weathering under low WI
153 implicitly encapsulates fluid travel times (via their dissolution/precipitation rate
154 parameterizations), suggesting that infiltration rates are too short to support active clay
155 precipitation, possibly due to thin soil mantles. Examples of fluid travel time controls on the
156 extent of $\delta^7\text{Li}_{\text{diss}}$ have also been demonstrated by previous reactive transport studies (Wanner and
157 others, 2014; Bohlin and Bickle, 2019; Golla and others 2021). We note, however, that
158 observations of low clay content in low WI environments may arise from reduced timescales for
159 accumulation due to short regolith residence times, rather than slow clay precipitation rates.
160 Here, we show that fluid travel time controls lead to a notable discrepancy between theories that
161 predict low $[\text{Li}^+]$ at low WI due to short fluid travel times, and observations that show the highest
162 $[\text{Li}^+]$ in low WI systems. To our knowledge, this discrepancy has not previously been articulated.

163 Specifically, observations of $[\text{Li}^+]$ in global rivers show the highest concentrations on the
164 order of $>10^3$ nM in low WI and rapidly eroding environments (Dellinger and others, 2015;
165 Pogge von Strandmann and Henderson, 2015), leading to a parabolic relationship between
166 $\delta^7\text{Li}_{\text{diss}}$ and $[\text{Li}^+]$, similar to that of $\delta^7\text{Li}_{\text{diss}}$ and WI (fig. 1). However, short fluid travel times and
167 reduced clay precipitation should theoretically limit overall primary mineral dissolution and the
168 subsequent accumulation of Li in solution, as balanced by reduced clay Li uptake. In fact, some
169 field sites do show the co-limitation of clay precipitation and associated primary mineral
170 dissolution under short fluid travel times, wherein high river discharge results in diluted $[\text{Li}^+]$
171 and low $\delta^7\text{Li}_{\text{diss}}$ values relative to baseflow (Lemarchand and others, 2010; Manaka and others,
172 2017).

173 Herein, we explore this apparent paradox and the links between weathering intensity and
174 congruence using a reactive transport model of lithium isotopes. Through the incorporation of
175 lithium isotope dynamics into the CrunchFlow reactive transport code (Steeffel and others 2015),
176 we expand on previous observational and theoretical formulations through the contemporaneous
177 representation of fluid flow (Maher 2010), multi-component mineral dissolution and
178 precipitation reactions (Steeffel and others, 2015), erosional forcing (Maher and Chamberlain,
179 2014), and isotope fractionation (Druhan and others, 2013; Wanner and others, 2014; Maher and
180 von Blanckenburg, 2016; Druhan and Winnick, 2019; Golla and others 2021). Simulations
181 across a range of weathering intensity scenarios are evaluated against observations of riverine
182 $\delta^7\text{Li}_{\text{diss}}$, making use of an update to the CrunchFlow software facilitating fractionating
183 precipitation and non-fractionating dissolution of a given mineral phase. We also explore the
184 transient evolution of weathering profiles under varying weathering intensities, along with the
185 potential role for changes in weathering zone mineralogy to influence observed lithium isotope
186 dynamics. While we acknowledge the broad and seminal applications of $\delta^7\text{Li}$ to study
187 weathering processes across the globe in many other studies, we restrict our data-model
188 comparison to data presented in Dellinger and others (2014, 2015, 2017) based on their
189 framework for interpreting $\delta^7\text{Li}$ signals as a function of Li/Al ratios. This normalization allows
190 comparison across a diversity of bedrock types.

191

192

METHODS

193

*Mineralogy and Geochemistry*194
195
196
197
198
199
200
201
202
203
204
205
206
207
208
209
210
211
212
213
214
215
216
217
218
219
220
221
222
223
224

In order to probe the relationships between weathering intensity, congruence, and $\delta^7\text{Li}$, we simulated upland weathering profiles using the reactive transport software CrunchFlow, making use of the isotope features developed in prior studies and a software update necessary to treat isotopes in systems of high weathering intensity. In CrunchFlow, mineral dissolution/precipitation rates are represented by Transition State Theory (TST)-style rate laws (cf. Lasaga, 1998) with a dependence on reaction affinity that allows dissolution/precipitation to occur only when solutes are under/over-saturated with respect to that given mineral phase, as

$$R_{net} = k_d * SA * \left(\frac{Q}{K_{eq}} - 1 \right) \quad (2),$$

where R_{net} is the net reaction rate for a specified mineral, k_d is a temperature-dependent intrinsic rate constant, SA is mineral surface area, Q is the ion activity product, and K_{eq} is the mineral equilibrium constant, and the $(Q/K_{eq} - 1)$ term represents reaction affinity. The composition of each solid phase is described as a stoichiometric and charge balanced assemblage of primary species, thus assuring mass balance between co-evolving dissolved solutes and solids.

One important effect of this affinity dependence is that it directly links the rate of primary mineral dissolution to the rate of secondary mineral precipitation. A common example is the precipitation of Al and Si to form secondary phases, which maintains undersaturated solute concentrations with respect to primary minerals bearing these elements (Zhu and others, 2005; Maher and others, 2006). Hence, the removal of weathering products into clay minerals allows mineral dissolution to continue by increasing the driving force for dissolution via the reaction affinity. This affinity dependence is not included in the regolith models that have primarily informed theoretical considerations of Li isotopes in previous studies (Chamberlain and others, 2005; Ferrier and Kirchner, 2008; Bouchez and others, 2013). In these models, variation in primary mineral dissolution occurs independent of clay precipitation, where the latter is parameterized as a constant rate. We note that these models were originally developed to track the evolution of solid-phase weathering zone mineralogy (Chamberlain and others, 2005; Ferrier and Kirchner, 2008). However, dissolved Li isotope compositions in these models are controlled by the relative kinetic rates of primary mineral dissolution and clay precipitation and are thus

225 uniquely sensitive to rate parameterizations (Bouchez and others, 2013). More recently, a
 226 CrunchFlow model was developed for Li isotope fractionation associated with an upland shale
 227 weathering profile (Golla and others 2021). This study demonstrated the functionality of explicit
 228 coupling between primary mineral dissolution and secondary mineral precipitation and
 229 successfully reproduced fluid $\delta^7\text{Li}$ profiles through the bedrock vadose zone and groundwater.

230 Here we generalize the approach taken in Golla and others (2021) using a representative
 231 granitic weathering profile simulated as in Maher (2011), with bedrock modeled as a
 232 combination of 60% volume quartz, 30% plagioclase feldspar (20% anorthite, 80% albite), and
 233 2% halloysite, leaving ~8% protolith porosity. Equilibrium constants were used primarily from
 234 the EQ3/EQ6 thermodynamic database (Wolery and others, 1990), supplemented with
 235 plagioclase equilibrium constants from Arnorsson and Stefansson (1999). Intrinsic rate constants
 236 and activation energies were taken from a compilation by Palandri and Kharaka (2004). Mineral
 237 reactions, kinetic rate constants (k_d), and equilibrium constants (K_{eq}) are shown in table 1, and
 238 we note that as in equation (2), affinity dependence is assumed to be linear for simplicity.

239 Additional simulations were conducted including a high solubility chlorite mineral at
 240 7.5% volume with quartz reduced to 52.5% to maintain porosity. We include these simulations
 241 as Li is often preferentially concentrated in ferro-magnesian minerals, substituting for Mg^{2+} and
 242 Fe^{2+} due to similar ionic radii (Tardy and others, 1972; Penniston-Dorland and others, 2017). We
 243 use the reaction stoichiometry and equilibrium constants for chlorite and intermediate weathering
 244 product vermiculite from Heidari and others (2017) based on constrained reactive transport
 245 simulations of weathering in the Shale Hills Critical Zone Observatory. We amend mineral
 246 stoichiometry such that Li^+ substitutes for Fe^{2+} . Additionally, we assume no fractionation during
 247 vermiculitization by enforcing the same $^7\text{Li}:$ ^6Li ratios in chlorite and vermiculite. We note that
 248 the choice of chlorite rather than other Li-rich soluble minerals such as lithium-bearing alkali
 249 amphiboles is primarily based on the existence well-established CrunchFlow reaction networks
 250 constrained by field studies (Heidari and others, 2017). However, the relationship between
 251 chlorite lithium dynamics and weathering intensity investigated here are theoretically
 252 transferrable to other highly soluble, lithium-rich minerals.

253

254

Lithium Isotope Parameterizations

255

256 Lithium isotopes were incorporated into these simulations by defining ${}^6\text{Li}$ and ${}^7\text{Li}$ as
 257 separate primary chemical species. To capture typical bedrock compositions, Li was
 258 incorporated into plagioclase minerals as a solid solution with Na, which offers a simple means
 259 of maintaining charge balance. The ${}^6\text{Li}$ and ${}^7\text{Li}$ values are set such that $\delta^{7}\text{Li}_{\text{bedrock}}$ is 0‰ and total
 260 concentration in our granitic mineral assemblage is ~ 40 ppm, within error of average upper
 261 continental crust (Teng and others, 2004). The inclusion of Li-rich chlorite in our mineral
 262 assemblage raises bedrock Li concentrations to ~ 60 ppm, more characteristic of shale
 263 concentrations (Holland, 1984) and bedrock within the low WI watersheds of the Beni river
 264 (Dellinger and others, 2015). Based on observations of stoichiometric dissolution of ${}^6\text{Li}$ and ${}^7\text{Li}$
 265 from primary silicate minerals, we assume no fractionation during dissolution, and ${}^6\text{Li}$ and ${}^7\text{Li}$
 266 are incorporated into a single mineral with a single K_{eq} and k_d value as shown in table 1.

267 To simulate fractionation during clay precipitation, we employ a solid-solution approach
 268 that consists of two isotopic end-member phases: ${}^6\text{Li}$ -Halloysite and ${}^7\text{Li}$ -Halloysite (Druhan and
 269 others, 2013). The coupled rate expressions for precipitation of these phases are,

$$271 \quad R_{6\text{Li-H}} = \frac{[{}^6\text{Li}^+]}{[{}^6\text{Li}^+ + {}^7\text{Li}^+]} * k_{6\text{Li-H}} * SA_H * \left(\frac{Q_{cc}}{K_{eq}} - 1 \right), \quad (3) \quad \text{and}$$

$$273 \quad R_{7\text{Li-H}} = \frac{[{}^7\text{Li}^+]}{[{}^6\text{Li}^+]} * \frac{[{}^6\text{Li}^+]}{[{}^6\text{Li}^+ + {}^7\text{Li}^+]} * \alpha_k * k_{6\text{Li-H}} * SA_H * \left(\frac{Q_{cc}}{K_{eq}} - 1 \right), \quad (4)$$

274
 275 where Q_{cc} is the total ion activity product (including ${}^6\text{Li}$ and ${}^7\text{Li}$) with respect to the combined
 276 halloysite phases, K_{eq} is the equilibrium constant (same for both phases), and α_k is the kinetic
 277 fractionation factor ($k_{7\text{Li-H}}/k_{6\text{Li-H}}$) after Druhan and others (2013) and Steefel and others (2014).
 278 As described in Steefel and others (2014), this formulation assumes that the isotopic composition
 279 of the solid phase does not play a role in fractionation during precipitation through the mineral
 280 isotopologue activities. Fractionation occurs solely as a result of specified differences in intrinsic
 281 rate constants between isotopologue clay phases. Thus, under appropriately simplified
 282 conditions, this model would create Rayleigh distillation-style fractionation in the $\delta^{7}\text{Li}_{\text{diss}}$ as $[\text{Li}^+]$
 283 is lost from solution due to clay precipitation. In other words, removal of Li from solution due to
 284 clay precipitation in the absence of primary mineral Li inputs would act as an open-system

285 process with a constant fractionation at far-from-equilibrium conditions, similar to Rayleigh
286 distillation.

287 In our simulations, we assume a kinetic fractionation factor of $\alpha_k = 0.982$ for
288 precipitation of the halloysite solid solution. This value is based on calculated fractionation
289 factors from upland environments in the Dellinger and others (2015) dataset and falls roughly in
290 line with experimental values (Vigier and others, 2008). As in previous modeling studies, this
291 fractionation is meant to encompass a range of potential processes including structural
292 substitution, interlayer exchange, and surface sorption (Bouchez and others, 2013; Wanner and
293 others, 2014). Notably, in our treatment, Li uptake by clay is simulated via charge balance with
294 Al (table 1), which is necessary within CrunchFlow. Rather than the direct structural substitution
295 of Li for Al, this parameterization is meant to reflect effective Li uptake by clays that includes
296 mechanisms such as sorption, interlayer exchange, and structural substitution.

297 The magnitude of observed fractionation in solutes is also controlled by the partition
298 coefficient for Li into clays, which reflects the ratio of lithium dissolved from primary minerals
299 that is incorporated into clays (P_{Li}) versus left in solution (f_{Li}) at equilibrium. Under this
300 formulation, $P_{Li} = (1 - f_{Li})$. The result is that isotopic signals in the dissolved phase are maximized
301 when almost all the lithium released via dissolution is incorporated into secondary precipitates.
302 To examine the sensitivity of fractionation to P_{Li} , we manually vary the concentration of clay Li
303 such that P_{Li} ranges from 0.01 to 0.99 (x values in table 1). Under this formulation, P_{Li} is equal to
304 the ratio of Li/Al in Halloysite to Plag(An₂₀) (that is, $P_{Li} = (x/2)/(0.0026/1.2)$). This range of P_{Li}
305 values is based on field observations of f_{Li} across South American watersheds, calculated from
306 ratios of Li/Al in suspended sediments to bedrock (Dellinger and others, 2015).

307 We chose to simulate a simple 1:1 clay phase (halloysite) rather than a suite of competing
308 clay phases including more complex 2:1 clays in order to maintain constant P_{Li} values within a
309 given model run. This reasoning also underlies our choice to represent an ‘effective’ clay uptake
310 rather than explicit representations of sorption, interlayer exchanges, and structural substitution.
311 Under these more complex representations, P_{Li} would necessarily vary within an individual
312 model run through time and with depth as the weathering reaction network evolved or Li actively
313 exchanged with clay phases. While these dynamics certainly impact Li during weathering, they
314 have not been adequately linked to mineral residence or fluid travel times in natural
315 environments, which are the primary focus of our analyses. Thus, any encapsulated links

316 between P_{Li} and erosion and flow rates would not be justified by previous literature. Our
 317 simplified representation allows us to isolate the impacts of erosion and flow rates across a range
 318 of set P_{Li} values and facilitates the direct comparison to Dellinger and others (2015, 2017)
 319 observations. As described above, these are based on Li/Al ratios in bedrock versus dissolved
 320 and suspended loads and thus also represent a composite suite of ‘effective’ uptake mechanisms.
 321 We note that x is the same within any given simulation for 6Li -Halloysite and 7Li -Halloysite such
 322 that fractionation is only induced by the kinetic fractionation factor. For simplicity, we assume
 323 that Li substitution at ppm levels does not impact K_{eq} values (Wang and Xu, 2001).

324
 325 *Software Update for Isotope Partitioning at High Weathering Intensity*

326
 327 As discussed above, the high weathering intensity regime requires that isotopically
 328 distinct secondary clays are ultimately re-dissolved into the fluid phase. However, equations (3)
 329 and (4) are not applicable under conditions where $\frac{Q_{cc}}{K_{eq}} < 1$ for the following reasons. First, the
 330 fractionation factor ($\alpha_k = 0.982$) would result in a more rapid reaction rate for the 6Li end-
 331 member relative to 7Li during dissolution. This would mean that the 6Li -bearing halloysite (eq.
 332 3) would dissolve faster than its counterpart, leading to spurious fractionation over the timescales
 333 considered here. Second, equations (3) and (4) contain no reference to the isotopic composition
 334 of the solid phase, and thus there is no ability to incorporate the isotope ratio of the halloysite
 335 that is being solubilized into the fluid phase within this framework. To address these issues, we
 336 use the version of the isotopic solid solution model originally developed in CrunchFlow (Druhan
 337 and others, 2013) where the solid solution ratio is based on the isotopic mole fractions of the
 338 mineral phase:

339
 340
$$R_{6Li-H} = Y_{6Li-H} * k_{6Li-H} * SA_H * \left(\frac{Q_{cc}}{Y_{6Li-H} * K_{eq}} - 1 \right), \quad (5) \text{ and}$$

341
 342
$$R_{7Li-H} = Y_{7Li-H} * \alpha_k * k_{6Li-H} * SA_H * \left(\frac{[{}^7Li^+]}{[{}^6Li^+]} \frac{Q_{cc}}{Y_{7Li-H} * K_{eq}} - 1 \right), \quad (6)$$

343

344 Where Y is the isotopic mole fraction or the number of moles of a given isotope of lithium per
 345 total number of moles of lithium in the halloysite phase.

346 To stoichiometrically dissolve halloysite that was originally formed following the
 347 coupled rate laws given in equations (3) and (4), we modify the original formulation of equations
 348 (5) and (6) such that the kinetic fractionation factor α_k is set to 1.0 (no fractionation) and thus the
 349 two minerals dissolve at the same relative rates. The result is that the isotope ratio of the neo-
 350 formed halloysite mineral will be delivered into the fluid phase, ensuring stoichiometric
 351 dissolution without spurious fractionation:

$$353 \quad R_{6Li-H} = \begin{cases} eq. 3, \frac{Q_{cc}}{K_{eq}} \geq 1 \\ eq. 5, \frac{Q_{cc}}{K_{eq}} < 1 \end{cases} \quad (7a) \text{ and}$$

$$354 \quad R_{7Li-H} = \begin{cases} eq. 4, \alpha_k = 0.982, \frac{Q_{cc}}{K_{eq}} \geq 1 \\ eq. 6, \alpha_k = 1.000, \frac{Q_{cc}}{K_{eq}} < 1 \end{cases} \quad (7b)$$

355 A similar approach was utilized in Golla and others (2021) for the development of a weathering
 356 profile model incorporating Li isotopes specifically to reproduce a measured dataset of vadose
 357 zone and groundwater samples.

358 *Weathering Scenarios*

359
 360 We simulate four separate weathering scenarios, sequentially increasing in complexity, to
 361 test the controls of weathering regimes on Li systematics as outlined in table 2.

- 362 • Scenario 1- Batch Reactor: we simulate batch reactor weathering reactions, to evaluate
 363 temporal trends in solute concentrations and to analyze the sensitivity of Li fractionation
 364 to Li congruence.
- 365 • Scenario 2- Chronosequence: we simulate a 1-D weathering profile chronosequence with
 366 no uplift/erosion to evaluate temporal trends in mineralogical and solute profiles.
- 367 • Scenario 3- Uplift/Erosion: we simulate 1-D weathering profiles with specified regolith
 368 production rates to test the controls of weathering intensity.
- 369 • Scenario 4- Uplift/Erosion with chlorite: we incorporate soluble, Li-rich chlorite into our
 370 1-D uplift/erosion profiles to test their potential controls on Li systematics.

371 Model set-up and boundary conditions are described in detail in the following subsections.

372

373 *Scenario 1 - Batch reactors:* To examine the general characteristics of our Li isotope
 374 parameterizations, we first simulate a simple batch reactor with no transport. These are
 375 initialized with an un-weathered primary mineral composition, dilute waters, a temperature of
 376 15° C, and fixed open-system $p\text{CO}_2$ of 5000 ppm, setting an initial pH of 5.0 that increases with
 377 progressive mineral dissolution/precipitation reactions. This $p\text{CO}_2$ choice is meant to reflect
 378 typical elevated values in soil environments due to oxidation of organic matter. We note that
 379 increased (decreased) $p\text{CO}_2$ leads to increased (decreased) equilibrium solute concentrations
 380 (Winnick and Maher, 2018), but does not influence isotopic evolution. Within these batch
 381 simulations, we vary the partition coefficient P_{Li} from 0.01 to 0.99 via x values as defined in
 382 *Lithium Isotope Parameterizations* and shown in table 1 for the halloysite phase. In each
 383 simulation, reaction progress is monitored for 5 kyr. We also demonstrate how the simulation of
 384 a 2:1 clay (Ca-beidellite) results in the same lithium fractionation dynamics as a function of P_{Li}
 385 as halloysite in Appendix A.

386

387 *Scenario 2 - Chronosequence:* Next, we simulate 1-D weathering profiles with no erosion to
 388 characterize the temporal evolution of solid and aqueous geochemical profiles. Weathering
 389 domains are set to 10 m with a grid cell size of 5 cm (200 cells). Initial porosity is set to 7%, and
 390 weathering occurs under 75% water saturation and a large prescribed gas flux of CO_2 into the
 391 domain to maintain open-system weathering conditions (Winnick and Maher, 2018). As in the
 392 batch simulations, profiles are initialized with an un-weathered primary mineral composition,
 393 dilute waters, a temperature of 15° C, and $p\text{CO}_2$ of 5000 ppm. Water infiltrates through the
 394 domain via Darcy flux with a prescribed rate of 0.5 m/yr. Simulations are run for 1 Myr, and
 395 changes in solid and aqueous geochemistry are analyzed at multiple timesteps.

396

397 *Scenario 3 - Uplift/Erosion:* We analyze the effects of variable weathering intensity by
 398 simulating 1-D weathering profiles with prescribed volumetric uplift/erosional forcing.
 399 CrunchFlow incorporates uplift/erosion through the specification of a volumetric uplift rate at the
 400 bottom of the domain equivalent to a regolith production rate. Material is removed from the top
 401 of the domain at the same volumetric rate; however, mass erosion rates are reduced relative to

402 regolith production due to chemical denudation of material before it is uplifted and removed at
403 the surface (fig. 1). Weathering domains, water saturation, and $p\text{CO}_2$ are set as in
404 chronosequence simulations. To examine the relationship between lithium isotope dynamics and
405 reactive transport, we simulated a suite of weathering regimes by varying infiltration and erosion
406 rates. Infiltration (Darcy flux) was varied between 0.1 to 5 m/yr, and regolith production
407 (volumetric erosion) was varied between 0.005 to 0.2 mm/yr, corresponding to erosion rates of
408 1.4 to 485 t/km²/yr after correcting for porosity changes during weathering (table 3), resulting in
409 30 unique weathering intensity regimes. Each weathering simulation was run for 0.5 Myr,
410 resulting in either the development of a steady-state profile (constant aqueous and solid
411 geochemical depth profiles) or transient profiles (time-dependent geochemical depth profiles
412 characterized by the progressive depletion of primary minerals). Model output was analyzed at
413 multiple timesteps to characterize the temporal evolution of mineral and solute profiles.

414 We define the regolith weathering zone within each time-step as model cells with >101%
415 initial bedrock porosity. This depth is meant to represent a conservative estimate of the
416 weathering front based on observable changes in bulk density (Maher and von Blanckenburg,
417 2016). We note that other modeling studies evaluate weathering depths based on solute
418 equilibrium length scales (Lebedeva and others, 2010), which in our simulations always occur
419 below the porosity-based weathering front. Our definition of weathering zone is meant to capture
420 potential contrasts in permeability that may affect subsurface flowpaths and travel times.
421 Specifically, due to the model setup which specifies constant Darcy flow, simulated water fluxes
422 do not vary within the profile domain based on porosity changes. To capture short fluid travel
423 times associated with preferential and interflow caused by thin regolith and sharp permeability
424 contrasts between weathered and fresh bedrock, we evaluate solute concentrations and $\delta^7\text{Li}_{\text{diss}}$ at
425 the base of this regolith weathering zone in addition to the base of the model domain. In the
426 simulations with low regolith production rates that result in weathering of the entire domain, we
427 evaluate solute concentrations at 9 m depth to avoid boundary condition effects associated with
428 the bedrock boundary condition at 10 m.

429 Model outputs and metric calculations are shown in table 3. Mass erosion rates are
430 calculated by multiplying the specified regolith production rate by bulk density in the top model
431 cell. Riverine suspended material is taken as the mineralogical composition of the eroding top
432 cell of the domain. Chemical denudation rate is calculated as the sum of major dissolved

433 weathering products ($[Ca^{2+}] + [Mg^{2+}] + [Na^+] + [K^+] + [SiO_{2(aq)}]$) multiplied by the prescribed
434 infiltration rate at both the domain boundary and at the bottom of the regolith weathering zone.
435 Finally, a metric of weathering incongruence (I) is calculated based on the ratio of the
436 instantaneous rate of halloysite precipitation to plagioclase dissolution ($I = -R_{halloysite}/R_{plagioclase}$;
437 as per equation (2), precipitation is a positive rate, and dissolution is a negative rate. This metric
438 is similar to qualitative descriptions of weathering incongruence under conditions of plagioclase
439 dissolution and halloysite precipitation, in which incongruence represents the molar ratio of clay
440 formation to primary mineral dissolution. When halloysite dissolves, however, incongruence is
441 calculated as a negative number.

442

443 *Scenario 4 – Uplift/Erosion with chlorite.*— To address the potential role of soluble, Li-rich
444 ferro-magnesian minerals such as chlorite in driving global δ^7Li_{diss} patterns, we conduct a series
445 of simulations including an amended chlorite mineral as shown in table 1. The weathering of
446 chlorite minerals involves a multi-step reaction series by which, first, cations in the octahedral
447 coordination layer (Mg^{2+} , Fe^{2+}) are leached in a process referred to as supergene
448 ‘vermiculitization’ (Proust and others, 1986). In general, this weathering step is not well-
449 characterized in field environments due to analytical challenges involved in distinguishing
450 unaltered chlorite and vermiculite. Recent studies, however, have made use of ratios of 7 Å to 14
451 Å XRD peaks along with stoichiometric characterizations to demonstrate vermiculitization in
452 deep regolith profiles (Sullivan and others, 2016; Gu and others, 2020). Following
453 vermiculitization, which may involve intermediate products of interstratified
454 chlorite/vermiculite, vermiculite products are further weathered to kaolinite-type clays.

455 To represent this multi-step process, we have included an intermediate, lower solubility
456 vermiculite mineral in addition to chlorite following the methodology of Heidari and others
457 (2017) (table 1). In terms of Li^+ , we assume no fractionation during ‘vermiculitization’ by
458 incorporating equivalent $^7Li^+ : ^6Li^+$ ratios in mineral stoichiometry. Further, we assume that Li^+
459 leaching relative to Al^{3+} falls intermediately between simulated leaching of Mg^{2+} and Fe^{2+} in
460 order to maintain realistic dissolved Li concentrations ($<10^4$ nM).

461 In these chlorite simulations, bedrock is initialized as 52.5% quartz, 30% plagioclase
462 (An₂₀), 7.5% ‘chlorite’ (6% chlorite, 1.5% vermiculite), and 2% halloysite. We note that these
463 mineral constituents are similar to quartz diorite in the Luquillo Critical Zone Observatory

464 (Murphy and others, 1997), whereas weathering fluxes from shale environments are more likely
465 to be dominated by chlorite, other clay minerals, with smaller amounts of plagioclase (Gu and
466 others, 2020). We conduct 1-D uplift/erosion weathering profiles under the same conditions as
467 described above.

468

469

RESULTS

470

471

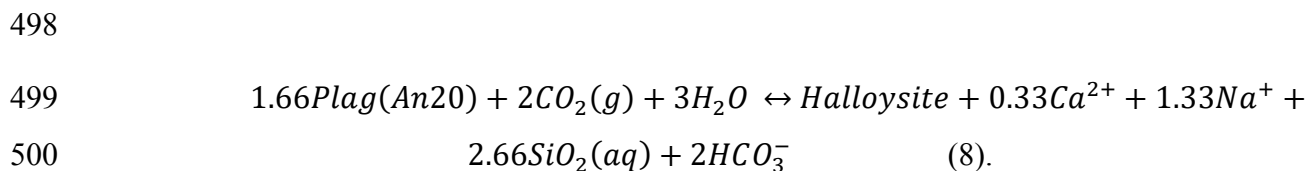
Batch Reactor Results (Scenario 1)

472

473 At the start of batch reactor simulations (Scenario 1), dilute waters are undersaturated
474 with respect to both plagioclase and halloysite, and primary mineral dissolution and secondary
475 mineral precipitation proceed as solute concentration profiles stabilize over roughly 10^2 years
476 (fig. 2). When the simulation begins, plagioclase dissolution is at its maximum rate, which is
477 sustained for the first ~ 6 months of simulation, representing kinetic controls. As solute
478 concentrations increase and waters approach saturation, a quasi-steady state develops in the
479 aqueous profiles and the affinity term in equation (2) becomes the limiting factor on dissolution
480 rates, which subsequently approach zero. We note that in these batch reactor scenarios,
481 plagioclase depletion is minimal, such that changes in surface area do not impact dissolution
482 rates through time (Eq. 2). Secondary mineral rates at the start of simulations denote net
483 dissolution, though at rates orders of magnitude slower than plagioclase dissolution, for the first
484 few days of simulation time as dilute solutes are undersaturated with respect to halloysite. As
485 Al^{3+} and $\text{SiO}_2(\text{aq})$ activities increase due to plagioclase dissolution, halloysite transitions to net
486 precipitation; however, due to the low intrinsic rate constant, net precipitation rates are initially
487 subdued. Precipitation rates increase to a maximum value roughly 2.5 months into the simulation
488 as solutes become orders of magnitude oversaturated with respect to halloysite and then
489 subsequently decrease over the rest of the simulation.

490 Instantaneous weathering incongruence is shown as the ratio of rates of halloysite
491 precipitation to plagioclase dissolution in figure 2b. At the start of the simulation, weathering is
492 fully congruent (ratio of zero) until the initiation of halloysite precipitation. Increasing halloysite
493 precipitation results in an overshoot in weathering incongruence, whereby more halloysite
494 precipitates than predicted based on equilibrium reaction stoichiometry to compensate for initial

495 congruent weathering. Following this overshoot, the ratio of halloysite precipitation to
 496 plagioclase dissolution approaches the stoichiometric balance of ~0.6 from the equilibrium
 497 reaction,



501
 502 We note that even as dissolution/precipitation rates decrease through time as the system
 503 approaches thermodynamic equilibrium, this stoichiometric ratio is maintained.

504 Simulated Ca^{2+} concentrations (fig. 2c) are influenced only by plagioclase dissolution, as
 505 Ca^{2+} is not incorporated into halloysite. Concentrations rise rapidly over the first ~6 months of
 506 simulation, after which increases attenuate as dissolution rates decrease. Maximum
 507 concentrations of ~45 μM are reached at roughly 500 years of simulation as the system
 508 approaches equilibrium, and this final concentration is dependent on the specified open-system
 509 $p\text{CO}_2$ through its control on initial and equilibrium pH (5.0 and 8.9, respectively) (Winnick and
 510 Maher, 2018). The evolution of Li^+ differs from Ca^{2+} due to the incorporation of Li^+ into
 511 precipitating halloysite. Concentrations are therefore strongly dependent on the partition
 512 coefficient (P_{Li}) as shown in fig. 2d. In the initial stages of weathering, Li^+ increases similarly
 513 across the range of partition coefficients, and after halloysite precipitation initiates, partition
 514 coefficient simulations diverge. Simulations with low partition coefficients in which relatively
 515 little of the Li^+ released during plagioclase dissolution is incorporated into halloysite result in
 516 rapidly increasing concentrations, similar to Ca^{2+} . In contrast, simulations with high partition
 517 coefficients result in a transient decrease in Li^+ reflecting the overshoot in weathering
 518 incongruence, followed by slowly increasing values as the system approaches equilibrium.

519 Partition coefficients also control the evolution of $\delta^7\text{Li}$ (fig. 3). When the partition
 520 coefficient is low and little Li^+ is incorporated into clays, the extent of fractionation is reduced,
 521 and $\delta^7\text{Li}_{\text{diss}}$ is similar to $\delta^7\text{Li}_{\text{plag}}$. When the partition coefficient is large, $\delta^7\text{Li}_{\text{diss}}$ reflects the full
 522 18‰ fractionation factor. Additionally, the transient weathering incongruence overshoot results
 523 in transiently elevated $\delta^7\text{Li}_{\text{diss}}$ values, which subsequently approach steady-state values. We note
 524 that, similar to instantaneous weathering incongruence, $\delta^7\text{Li}_{\text{diss}}$ reach steady-state values at
 525 roughly 6 months, which is long before the system as a whole approaches equilibrium. Rather

526 than overall reaction progress, $\delta^7\text{Li}_{\text{diss}}$ reflects the approach to stoichiometric balance between
527 plagioclase dissolution and halloysite precipitation.

528 In figure 3b, we show the relationship between $\delta^7\text{Li}_{\text{diss}}$ and f_{Li} , which in this case reflects
529 the weathering congruence of Li^+ (combining both congruence changes in the approach to
530 stoichiometric balance and P_{Li}). Steady-state $\delta^7\text{Li}_{\text{diss}}$ values (colored circles reflecting plateau
531 values in fig. 3a) are linearly related to f_{Li} , similar to the ‘batch-reactor’ relationship described by
532 Bouchez and others (2013) and Dellinger and others (2015). The approach to steady-state $\delta^7\text{Li}_{\text{diss}}$
533 values within each P_{Li} simulation (colored lines) involves a stronger dependence on f_{Li} than
534 steady-state values, which is due to the previously described overshoot in halloysite precipitation
535 rates and weathering incongruence. Global riverine $\delta^7\text{Li}_{\text{diss}}$ observations from Dellinger and
536 others (2015) are also shown and fall roughly in line with CrunchFlow simulations, with the
537 exception of flood-plain dominated environments as described above, which require sustained
538 open-system clay uptake as in Maffre and others (2020).

539

540 *Weathering Profiles – Chronosequence (Scenario 2)*

541

542 Reactive transport simulations of weathering profiles have been presented in a number of
543 previous studies (Maher and others, 2009; Maher, 2010, 2011; Moore and others, 2012;
544 Lebedeva and Brantley, 2013; Lawrence and others, 2014; Pandey and Rajaram, 2016; Heidari
545 and others, 2017; Winnick and Maher, 2018; Jung and Navarre-Sitchler, 2018; Perez-Fodich and
546 Derry, 2019; Golla and others 2021). We limit this discussion to a brief overview of general
547 weathering characteristics and refer readers to these references for further details. Results from
548 our simulations are shown in figure 4 with a P_{Li} value of 0.9, where colored lines are used to
549 represent the evolution of solid and aqueous profiles through time.

550 At the beginning of the simulation, the solid profile represents fresh, unweathered
551 bedrock. For this choice of initial conditions, the spatial evolution of aqueous solutes and mineral
552 reaction rates generally resemble the temporal evolution of the batch reactor experiments
553 presented above. Plagioclase weathering begins immediately at the surface as dilute, weakly
554 acidic (pH = 5.0) waters infiltrate, releasing Ca^{2+} and Li^+ (along with other reaction products not
555 shown) into solution. Halloysite precipitation begins at ~20 cm depth, reflecting the water travel
556 times necessary to significantly oversaturate solutes with respect to halloysite, as in figure 2a.

557 This balance of dissolution/precipitation is reflected in weathering incongruence (fig. 4c), where
558 incongruence increases at the depth where halloysite precipitation becomes significant, reaches a
559 maximum at ~ 0.75 m, and approaches the stoichiometric balance of plagioclase dissolution to
560 halloysite precipitation (0.6) at roughly 2 m. As with the batch reactor experiments (fig. 3a),
561 $\delta^7\text{Li}_{\text{diss}}$ tracks weathering incongruence, approaching enriched steady-state values at ~ 1 m (fig.
562 4f).

563 As the simulation moves through time, plagioclase is progressively depleted from the
564 shallow depths, with this pattern propagating downward through the profile. Plagioclase is
565 largely depleted from the 10 m weathering profile by the end of the simulation at 10^6 yrs;
566 however, small amounts remain as the surface area term in equation (2) limits kinetic rates of
567 dissolution. Halloysite builds up in the profile from top to bottom due to progressive
568 precipitation, though, precipitation is limited in the top 20 cm due to slow kinetics. Additionally,
569 halloysite transitions to dissolution when plagioclase is sufficiently depleted at the top of the
570 profile. Solute profiles of $[\text{Ca}^{2+}]$ and $[\text{Li}^+]$ generally track the evolution of mineral profiles on
571 these long timescales. Specifically, decreases in $[\text{Ca}^{2+}]$ and $[\text{Li}^+]$ at a given depth through time
572 match plagioclase depletion and are related to reduced mineral surface area and subsequent
573 decreasing dissolution rates.

574 Weathering incongruence and subsequent $\delta^7\text{Li}_{\text{diss}}$ approach steady-state values at
575 increasing depths through time. This is tied to reduced plagioclase dissolution rates in the upper
576 profile as primary mineral is depleted, resulting in greater travel times needed to initiate
577 halloysite precipitation and approach $\delta^7\text{Li}_{\text{diss}}$ steady-state values. Despite these longer $\delta^7\text{Li}_{\text{diss}}$
578 length scales, steady-state values are approached by the bottom of the 10 m profile until
579 plagioclase is depleted throughout the profile at 10^6 yrs. When plagioclase has been depleted, the
580 weathering regime transitions to net clay dissolution throughout the profile, and $\delta^7\text{Li}_{\text{diss}}$ values
581 become more negative, resembling the clay values that were precipitated earlier in the
582 simulation. However, through time, very small rates of plagioclase dissolution cause $\delta^7\text{Li}_{\text{diss}}$ to
583 evolve during transport and fall between bedrock and clay values by the bottom of the profile.
584 This last timestep also coincides with low $[\text{Li}^+]$ due to slow dissolution kinetics of halloysite.
585 These results are consistent with some behavior shown in tropical weathering environments
586 (Lara and others, 2022) in which $\delta^7\text{Li}_{\text{diss}}$ are extremely low in weathered soils (though absolute
587 values of measured pore waters and clay $\delta^7\text{Li}$ would require extremely low P_{Li} values and large

588 clay fractionation) and are disconnected from stream environments as deeper weathering and
 589 higher $[\text{Li}^+]$ from primary mineral dissolution seemingly overwhelm clay dissolution.

590

591 *Uplift/Erosion (Scenario 3)*

592

593 As described previously, we simulate a range of both uplift/erosion and flow rates to
 594 capture a broad range of weathering intensity regimes. Across this suite, 30 unique WI regimes
 595 were tested, varying from 2.7×10^{-5} to 0.93. Illustrative examples of low weathering intensity
 596 (high uplift/erosion, low flow), moderate weathering intensity (comparable uplift/erosion and
 597 flow), and high weathering intensity (low uplift/erosion, high flow) environments are compared
 598 in figure 5. We note that in figure 5, only the low weathering intensity simulation reaches steady-
 599 state with respect to the mineral abundances and fluid compositions, as discussed below.

600 Under low weathering intensity, the supply of fresh bedrock overwhelms chemical
 601 denudation, and weathering profile solid compositions reflect bedrock values throughout the
 602 simulation (fig. 5a–c). In the illustrative example, plagioclase is very slightly depleted within the
 603 top <1 m. Based on our definition of the regolith weathering zone (porosity >101% bedrock
 604 porosity), this profile corresponds to a regolith depth of 5 cm, and solute concentrations are taken
 605 from this depth when comparing between weathering intensity simulations. Similar to solid
 606 composition, weathering incongruence and $\delta^7\text{Li}_{\text{diss}}$ profiles do not vary significantly with depth
 607 or through the course of the simulation. As water infiltrates through the 1D un-weathered
 608 bedrock profile, the behavior is largely comparable to the batch reactors; however, the approach
 609 to stoichiometric weathering incongruence and steady-state $\delta^7\text{Li}_{\text{diss}}$ values occur at depths below
 610 the defined regolith weathering zone. As a result, $\delta^7\text{Li}_{\text{diss}}$ values from this simulation are $\sim 0\%$ at
 611 the weathering zone depth of 5 cm.

612 When erosion rates and chemical denudation are comparable under moderate weathering
 613 intensity, weathering profiles evolve with depth throughout the duration of the simulation.

614 Through time, plagioclase is depleted and halloysite is precipitated in the upper portion of the
 615 profile. In contrast to the no-erosion simulation in figure 4, plagioclase reaction fronts are
 616 condensed, reflecting the additional uplift flux of bedrock. Similarly, the erosion of material
 617 from the surface eliminates the diminished accumulation of halloysite in the top few cm's of the
 618 profile as compared to figure 4. In figure 5(e–h), regolith depth reaches a maximum of ~ 8 m in

619 10⁶ yrs. As with the no-erosion case, weathering incongruence and $\delta^7\text{Li}_{\text{diss}}$ track the evolution of
 620 the solid profile, with an increasing length needed to approach stoichiometric incongruence and
 621 steady-state $\delta^7\text{Li}_{\text{diss}}$ values. Throughout the simulation, both incongruence and $\delta^7\text{Li}_{\text{diss}}$ approach
 622 steady-state maximum values at the base of the weathered regolith profile. At 10⁶ years when
 623 plagioclase is completely depleted from the top of the profile, clay dissolution occurs over the
 624 top ~1 m during infiltration; however, the associated low $\delta^7\text{Li}_{\text{diss}}$ values are quickly overwhelmed
 625 by the influx of lithium when waters reach the plagioclase dissolution front.

626 Under high weathering intensity, the lack of uplift/erosional forcing results in the
 627 depletion of primary minerals and accumulation of secondary minerals as shown in figure 5(i-l).
 628 We note that while patterns resemble those presented in figure 4, a few differences exist largely
 629 related to differences in infiltration rate (5 m/yr in fig. 5 v. 0.5 m/yr in fig. 4). As a result of these
 630 high infiltration rates, overall weathering intensity increases, causing plagioclase depletion
 631 almost uniformly throughout the profile rather than in a discrete reaction front. Another
 632 important difference is the approach to bedrock conditions at 10 m depth, which reflects the
 633 imposed uplift/erosion boundary condition. Similar to figure 4, weathering incongruence profiles
 634 track the solid profile composition. At early time, weathering incongruence remains low over the
 635 first ~1 m of infiltration before approaching stoichiometric incongruence coincident with the
 636 approach to steady-state $\delta^7\text{Li}_{\text{diss}}$ values; this is due to fast infiltration rates which result in reduced
 637 water travel times in comparison to figure 4. At simulation time 10⁵ yrs, very little plagioclase
 638 remains throughout the profile. As a result, while weathering incongruence reaches
 639 stoichiometric balance by the bottom of the profile, overall plagioclase dissolution rates and
 640 subsequent Li release from primary minerals are so low that $\delta^7\text{Li}_{\text{diss}}$ reflects a mixture of
 641 halloysite dissolution at the top of the profile (negative incongruence) and plagioclase
 642 dissolution/halloysite precipitation at the bottom. Following the complete denudation of
 643 plagioclase from the upper profile by 2.5x10⁵ yrs, weathering incongruence and $\delta^7\text{Li}_{\text{diss}}$ remain
 644 low throughout the profile.

645

646

Erosion/Uplift with Chlorite (Scenario 4)

647

648

649

The introduction of soluble chlorite minerals changes lithium weathering dynamics within our simulations. In these simulations, the rapid vermiculitization of chlorite releases Li

650 congruently. As a result, dissolved Li concentrations are high ($\sim 1 \mu\text{M}$), and $\delta^7\text{Li}_{\text{diss}}$ values are
651 close to bedrock values when chlorite is present. Plagioclase dissolution and subsequent
652 halloysite precipitation continue to a reduced degree in the presence of chlorite but have little
653 effect on Li concentrations and isotopes due to the relatively small amount of Li released and
654 removed in comparison to vermiculitization.

655 The temporal evolution of 1-D weathering profiles with chlorite can be seen in the high
656 weathering intensity panels in figure 6. Due to its high solubility, chlorite is rapidly weathered to
657 vermiculite, involving the leaching of Mg^{2+} and Li^+ throughout the weathering profile over
658 <1000 years of simulation. When chlorite is present in the profile, Li concentrations are high and
659 $\delta^7\text{Li}_{\text{diss}}$ resemble bedrock values. However, after the rapid depletion of chlorite, the high
660 weathering intensity simulations behave similar to those in figure 5(i-l). Plagioclase is depleted
661 from the profile over timescales of 10^5 yrs, after which clay dissolution is the primary contributor
662 to Li concentrations and $\delta^7\text{Li}_{\text{diss}}$.

663 Similar dynamics are observed under moderate weathering intensity (fig. 6 e-h). Despite
664 elevated uplift/erosion rates relative to the high weathering intensity simulation, protolith chlorite
665 is still depleted from the profile in $<10^5$ years. As before, once chlorite is depleted, the temporal
666 evolution of the profile behaves as in figure 5(e-h), in which incongruent plagioclase weathering
667 leads to high $\delta^7\text{Li}_{\text{diss}}$ values and Li concentrations on the order of 10^2 nM, both of which are
668 dependent on P_{Li} .

669 In the low weathering intensity scenario, uplift/erosion rates are sufficiently high that
670 significant chlorite mineral concentrations remain within the weathering zone throughout the
671 simulation (fig. 6 a-d). In other words, under high enough uplift/erosion and low enough water
672 infiltration rates, chlorite becomes kinetic- rather than supply limited. As a result, Li
673 concentrations remain high ($\sim 10^3$ nM) and $\delta^7\text{Li}_{\text{diss}}$ reflect bedrock values throughout 1 Myr of
674 simulation within the shallow weathering zone.

675 These results are broadly consistent with field studies demonstrating deep chlorite
676 ‘vermiculitization’ or the leaching and oxidative weathering of octahedral cations (Mg^{2+} , Fe^{2+})
677 relative to plagioclase depletion depths under low to moderate erosion rates, along with the
678 presence of fresh chlorite in shallow soils under high erosion rates (Sullivan and others, 2016;
679 Gu and others, 2020). Mineralogic profiles in tropical weathering environments have also

680 demonstrated the complete depletion of chlorite in weathered saprolite and soil (Murphy and
681 others, 1998).

682

683 *Weathering Intensity, $\delta^7\text{Li}$, and $[\text{Li}^+]$*

684

685 In figure 7, we compare the relationships among $\delta^7\text{Li}_{\text{diss}}$ and both weathering intensity
686 and $[\text{Li}^+]$ from Scenarios 3 and 4 and global observations from Dellinger and others (2015) and
687 references therein. Figure 7 shows model output at the 500,000-year timestep for simulations
688 with a P_{Li} value of 0.9 (maximum isotopic offset of $\sim 17\%$). We also discuss the sensitivity of
689 model results to variable P_{Li} values in Appendix A. This timestep choice allows for the
690 development of deeply weathered profiles under low erosion conditions, characteristic of tropical
691 craton environments; at earlier timesteps, many high WI simulations have not fully transitioned
692 to clay dissolution. In both our simulations without and with the inclusion of chlorite, $\delta^7\text{Li}_{\text{diss}}$
693 follows a parabolic pattern with low (bedrock-like) values at both high and low weathering
694 intensity. In agreement with observations and as previously theorized, low $\delta^7\text{Li}_{\text{diss}}$ at high
695 weathering intensity is due to long mineral residence times that result in the depletion of primary
696 minerals and the dominance of secondary mineral dissolution across both classes of simulation.
697 However, despite similar $\delta^7\text{Li}_{\text{diss}}$ values at low weathering intensity, the mechanisms underlying
698 this behavior vary between simulations. When chlorite is not included in our mineral
699 assemblage, low weathering intensity $\delta^7\text{Li}_{\text{diss}}$ values are due to rapid fluid travel times through
700 the shallow weathering zone that limit secondary mineral precipitation. In contrast, low
701 weathering intensity $\delta^7\text{Li}_{\text{diss}}$ values with the inclusion of chlorite are caused by the active
702 weathering of soluble, Li-rich minerals which overcome clay precipitation uptake and are
703 sustained only through the rapid uplift supply of fresh bedrock.

704 As a result of these differing mechanisms, the relationships between $\delta^7\text{Li}_{\text{diss}}$ and $[\text{Li}^+]$
705 differ between the two classes of simulation. When chlorite is not included, $\delta^7\text{Li}_{\text{diss}}$ is low at low
706 $[\text{Li}^+]$ and high at high $[\text{Li}^+]$. Under high weathering intensities when clay dissolution dominates
707 Li release, low clay solubilities and lack of a precipitating phase result in low $[\text{Li}^+]$ and $\delta^7\text{Li}_{\text{diss}}$.
708 Under low weathering intensities, fluid travel time limitations on secondary mineral precipitation
709 also limit primary mineral dissolution, and $[\text{Li}^+]$ is unable to accumulate. Only under moderate
710 weathering intensities when incongruent weathering (eq. 8) can occur within the weathering zone

711 does $[\text{Li}^+]$ approach equilibrium concentrations; however, we note that even these $[\text{Li}^+]$ values
712 are roughly an order of magnitude less than maximum riverine $[\text{Li}^+]$ observations. When chlorite
713 is included, simulations produce the observed parabolic relationship between $\delta^7\text{Li}_{\text{diss}}$ and $[\text{Li}^+]$, as
714 the dissolution of chlorite at low weathering intensities allows for $[\text{Li}^+]$ to accumulate in solution
715 and approach the range of maximum observed $[\text{Li}^+]$ values (10^3 nM).

716 Lastly, figure 8 shows simulated $\delta^7\text{Li}_{\text{sus}}$, taken as the isotopic composition of lithium in
717 plagioclase and halloysite (and chlorite when included) in the eroding uppermost model domain
718 cell (0.025 m) at the 250 ka time-step, in comparison to values from Dellinger and others (2017).
719 We exclude low-Li quartz eroded from the surface in our calculation, as Dellinger and others
720 (2017) report values from the fine fraction of sediment. Figure 8 shows results from both classes
721 of simulation (with and without chlorite), between which the overall pattern does not vary. At
722 low weathering intensity, the erosion of minimally-weathered bedrock from the profile surface
723 results in bedrock-like $\delta^7\text{Li}_{\text{sus}}$ values that vary across our simulations based on initialized $\delta^7\text{Li}$
724 values of halloysite in bedrock. Above weathering intensities of ~ 0.01 , plagioclase (and chlorite)
725 is increasingly depleted from eroding surfaces in our simulations. As a result, $\delta^7\text{Li}_{\text{sus}}$ values
726 decrease, approaching $\delta^7\text{Li}$ values of precipitating clay, which are dependent on P_{Li} .
727 Observational data follow this general trend as well, with low $\delta^7\text{Li}_{\text{sus}}$ values at high weathering
728 intensity falling roughly in the center of our simulation ranges.

729

730

DISCUSSION

731

732 The results from our series of CrunchFlow weathering simulations suggest a number of
733 important controls on Li systematics and their relationship to weathering regimes. We first
734 compare model output to global river observations and review the primary drivers of Li isotope
735 and concentration signals including weathering congruence, mineral composition, mineral
736 residence times in regolith, and fluid travel times. Next, we discuss the inability of fluid travel
737 time controls to capture observed relationships between weathering regime, $\delta^7\text{Li}_{\text{diss}}$, and $[\text{Li}^+]$.
738 Instead, we show that the incorporation of soluble, Li-rich chlorite phases in our weathering
739 experiments produces signals consistent with global observations. Additionally, we describe an
740 alternative hypothesis outside the scope of CrunchFlow simulations that geothermal water
741 contributions may also link weathering regimes and Li isotopes and concentrations in river

742 systems. Lastly, we discuss model limitations along with need for future studies to evaluate these
743 hypotheses in the field.

744

745 *Insights from Reactive Transport Simulations*

746

747 With a relatively simple representation of kinetic lithium isotopic fractionation during
748 clay precipitation, we are able to capture a number of key features of global riverine Li data.
749 First, as shown in figure 3, the simulated offset between $\delta^7\text{Li}_{\text{diss}}$ and $\delta^7\text{Li}_{\text{bedrock}}$ is a function of the
750 fraction of Li dissolved that remains in solution, f_{Li} . This relationship is linear, matching general
751 ‘batch reactor’-style behavior observed across the Amazon basin (Dellinger and others, 2015).
752 As our analysis is focused on hillslope processes, we do not simulate the scavenging of dissolved
753 Li by extant secondary phases as is theorized to occur in floodplains. The result is that we do not
754 capture significantly elevated $\delta^7\text{Li}_{\text{diss}}$ values (20‰–35‰), attributed to ‘Rayleigh-style’
755 floodplain processes (fig. 3b), though transient overshoots in weathering incongruence during
756 initial clay precipitation capture similar style behavior.

757 Our relatively simple weathering mineralogy is also able to capture global ranges of
758 riverine $[\text{Li}^+]$ from $\sim 10^0$ to 10^3 nM, though we note that simulated concentrations above 200 nM
759 require the inclusion of a soluble, Li-rich mineral such as chlorite or lithium-bearing alkali
760 amphibole. In particular, across simulations both with and without chlorite, the transition from
761 clay dissolution to primary mineral dissolution between high and medium weathering intensity
762 environments captures the observed increase in $[\text{Li}^+]$ from $\sim 10^0$ to $\sim 10^2$ nM along with decreases
763 in $\delta^7\text{Li}_{\text{diss}}$ values. Simulations with high chlorite-derived $[\text{Li}^+]$ are discussed in more detail in the
764 following section.

765 Our simulations also clarify the distinct controls of fluid travel time and mineral
766 residence time on Li systematics. Similar to previous reactive transport studies, $\delta^7\text{Li}_{\text{diss}}$ during
767 incongruent weathering increases with increasing fluid travel time (Wanner and others, 2014;
768 Bohlin and Bickle, 2019; Golla and others 2021). We note, however, that our simulations reach
769 maximum $\delta^7\text{Li}_{\text{diss}}$ as incongruent weathering approaches a stoichiometric steady-state, while
770 solute concentrations continue to increase. This occurs on much shorter timescales than those
771 required for the system to approach a meta-stable equilibrium between dissolving and
772 precipitating phases when net reaction rates approach zero and solute concentrations remain

773 constant. This travel time dependence broadly matches concentration-discharge behavior
774 observed in streams, in which high seasonal discharge periods associated with faster fluid travel
775 times exhibit lower $[\text{Li}^+]$ and $\delta^7\text{Li}_{\text{diss}}$ as compared to low discharge periods (Lemarchand and
776 others, 2010; Manaka and others, 2017). We demonstrate qualitative concentration-discharge
777 dynamics associated with our model output assuming a gamma-function travel time distribution
778 in Appendix B.

779 In contrast, mineral residence times control the dominant weathering reactions, as
780 primary minerals are sequentially depleted from regolith with increasing mineral residence time.
781 This has previously been suggested to control the transition from primary mineral dissolution to
782 secondary mineral dissolution at high weathering intensities (Bouchez and others, 2013), and we
783 extend this framework to demonstrate potential transitions in dominant primary mineral reactions
784 and associated Li sources at low weathering intensities. We also note that mineral residence
785 times do not directly impact weathering congruence in our simulations except through these
786 distinct transitions in weathering mineralogy. This is in contrast to previous studies in which
787 relative rates of primary mineral dissolution and secondary mineral precipitation are directly
788 dependent on mineral residence times (Chamberlain and others, 2005; Ferrier and Kirchner,
789 2008; Bouchez and others, 2013). While halloysite does not significantly accumulate under short
790 mineral residence times within our low WI simulations (fig. 5b), relative rates of halloysite
791 precipitation are still proportional to plagioclase dissolution integrated across the modeling
792 domain as enforced through the affinity-dependence terms in mineral precipitation/dissolution
793 rates (eq. 2). We offer a linkage between mineral residence time controls, fluid travel times and
794 associated weathering congruence by evaluating solute exports from the defined regolith zone
795 (gray shading in fig. 5 and 6), representing preferential flow through more porous regolith and
796 soil media relative to unweathered bedrock. This connection is implicit in previous studies, and
797 we discuss its incompatibility with observations of high $[\text{Li}^+]$ under low WI in the following
798 section.

799 CrunchFlow simulations also support the hypothesis that mineral residence times are
800 responsible for the broad trends between observed $\delta^7\text{Li}_{\text{sus}}$ and weathering intensity (Dellinger
801 and others, 2017; fig. 8). Specifically, at low weathering intensities when mineral residence
802 times are short, $\delta^7\text{Li}_{\text{sus}}$ largely represents contributions from primary minerals as interpreted by
803 Dellinger and others (2017). With increasing weathering intensity and the depletion of primary

804 minerals from the shallow, actively-eroding zone of regolith, $\delta^7\text{Li}_{\text{sus}}$ transitions to values
805 reflecting secondary minerals. We note that our simulations predict a much wider spread in
806 $\delta^7\text{Li}_{\text{sus}}$ at high weathering intensities than observed. This primarily reflects the fact that low
807 $(\text{Li}/\text{Al})_{\text{sec}}/(\text{Li}/\text{Al})_{\text{prim}}$ (that is, P_{Li}) are not observed at low weathering intensities (Dellinger and
808 others, 2017).

809

810 *Weathering Intensity Controls on $\delta^7\text{Li}_{\text{diss}}$*

811

812 As described by both observations and theoretical considerations, $\delta^7\text{Li}_{\text{diss}}$ is related to WI
813 through a parabolic relationship (fig. 1, fig. 7e). Previous studies hypothesize that low $\delta^7\text{Li}_{\text{diss}}$
814 values observed in low WI environments are caused by short fluid and mineral residence times
815 that inhibit secondary mineral precipitation relative to primary mineral dissolution, thereby
816 limiting the extent of Li fractionation (Bouchez and others, 2013; Dellinger and others, 2015).
817 Our CrunchFlow simulations demonstrate two potential issues with this hypothesis. First, the
818 treatment of weathering profiles within a multi-component RTM framework in which reaction
819 rates are based on solution chemistry suggests that there is no intrinsic connection between
820 mineral residence time and weathering congruence. Models that include this connection
821 implicitly assume that all weathering occurs within regolith, or mineral-depleted weathering
822 profiles, such that travel times are dependent on regolith thickness. However, this does not
823 account for infiltration of waters into relatively un-weathered bedrock, for example via fracture
824 flow. As shown in Appendix B, riverine $\delta^7\text{Li}_{\text{diss}}$ may reflect a lack of secondary mineral
825 precipitation depending on the travel time distributions and mean travel times that dictate the
826 proportional contribution of these ‘young’, non-evolved waters (Kirchner, 2016; Jasechko and
827 others, 2016). However, for travel times to result in the observed $\delta^7\text{Li}_{\text{diss}}$ -WI relationships, young
828 water fractions would need to be highest in low WI environments. This connection between
829 travel times and erosional environments is an open question; however, we note that this is in
830 direct contrast to Jasechko and others (2016), who suggest relatively low proportions of ‘young’
831 waters in high slope environments associated with low WI.

832 Second, short fluid travel times that limit secondary mineral precipitation also limit
833 primary mineral dissolution and overall reaction progress. The result is that under short fluid
834 travel times, simulated $[\text{Li}^+]$ is extremely low, on the order of <10 nM. This is in direct conflict

835 with observations that show the highest $[\text{Li}^+]$ in low WI and rapidly eroding environments, on
836 the order of 10^3 nM (Dellinger and others, 2015; Pogge von Strandmann and Henderson, 2015).
837 Fluid travel times, are therefore unable to capture observed parabolic relationships between
838 $\delta^7\text{Li}_{\text{diss}}$ and $[\text{Li}^+]$ as shown in figure 7. Given that observed low WI $[\text{Li}^+]$ on the order of 10^3 is
839 difficult to account for with typical granitic Li concentrations and plagioclase mineral solubility,
840 we suggest that low WI observations instead represent Li release from soluble, Li-rich minerals
841 such as chlorite.

842 Under this hypothesis, only low WI and short mineral residence times within the
843 weathering zone are able to maintain chlorite in significant concentrations. Our simulated
844 chlorite weathering profiles broadly match a recent comparison of ‘vermiculitization’ profiles
845 under high, medium, and low erosion rates in which protolith chlorite concentrations are
846 maintained in shallow soils only under high erosion rates (1–3 mm/yr; Gu and others, 2020). Due
847 to the high solubility and relatively high Li concentrations of chlorite, low $\delta^7\text{Li}_{\text{diss}}$ results from
848 high dissolved Li concentrations that overwhelm uptake by secondary mineral precipitation. In
849 our simulations, the transition from low to moderate weathering intensity then results in a change
850 in the dominant Li weathering reaction from chlorite dissolution to plagioclase dissolution,
851 which is an inherently more incongruent weathering reaction for Li. This mechanism, in contrast
852 to fluid travel times, predicts parabolic relationships between $\delta^7\text{Li}_{\text{diss}}$ and both WI and $[\text{Li}^+]$
853 consistent with observations, as shown in figure 7. We note that while our simulations are
854 limited to idealized representations of chlorite leaching, this overall pattern is characteristic of a
855 general situation in which Li exists at relatively higher concentrations in a more soluble mineral
856 within the bedrock assemblage such as lithium-bearing alkali amphiboles.

857 We also suggest that while our simulations only involve steady surface erosion rates,
858 these dynamics should theoretically apply to environments in which transient mass wasting
859 events occur as well. Periodic mass wasting events would expose fresh bedrock and allow for
860 highly weatherable minerals to be maintained close to the surface.

861 With respect to riverine observations, low WI primarily represents the weathering of
862 shale (Dellinger and others, 2015; Beni River) and metamorphically-altered (Pogge von
863 Strandmann and Henderson, 2015; New Zealand) bedrock, which typically contain Li-rich, ferro-
864 magnesian minerals such as chlorite. As mentioned above, the inclusion of chlorite brings our
865 bedrock Li concentrations in line with typical shale values (Holland, 1984) and bedrock values

866 observed in the Beni River watershed (Dellinger and others, 2015). Further, a study of Amazon
 867 tributary sediments found high stream chlorite and illite contents (~30%) in the Andean Madeira
 868 River (of which the Beni is a tributary) suggesting rapid erosion of soluble minerals (Gibbs,
 869 1967). Additionally, chlorite presence decreases significantly along the Andean Ucayali river
 870 and is significantly lower in Amazon shield rivers (Irion, 1983; Gibbs, 1967), also in line with
 871 our hypothesized mineralogic controls. While we demonstrate the potential for chlorite
 872 weathering to explain observed relationships between weathering intensity, $\delta^7\text{Li}_{\text{diss}}$, and $[\text{Li}^+]$,
 873 only very limited inferences have been drawn regarding chlorite contributions to Li weathering
 874 in actively eroding field environments (Golla and others 2021). Thus, targeted studies are needed
 875 to evaluate whether or not chlorite or other highly soluble, Li-bearing minerals are responsible
 876 for high $[\text{Li}^+]$ and low $\delta^7\text{Li}_{\text{diss}}$ in low WI environments. Other mechanisms such as geothermal
 877 water contributions may also be consistent with the parabolic relationships in figure 7(e–f), as we
 878 describe in the following section.

879

880

Alternative Hypothesis: Geothermal Waters

881

882 Our analysis confirms that changes in weathering zone mineralogy as modulated by
 883 weathering intensity are consistent with global patterns of riverine lithium concentrations and
 884 isotopes; however, other mechanisms may also contribute to observed patterns. One possibility is
 885 that geothermal waters play an increasingly important role in Li fluxes under low weathering
 886 intensity conditions. A number of studies have observed high $[\text{Li}^+]$ (10^{-1} – 10^4 μM) often
 887 coincident with bedrock-like $\delta^7\text{Li}_{\text{diss}}$ values in geothermal springs (Millot and Negrel, 2007;
 888 Millot and others, 2007, 2010b, 2012; Bernal and others, 2014; Godfrey and Álvarez-Amado,
 889 2020). This has been attributed to high reaction temperatures that alter dominant clay stability to
 890 phases that incorporate less Li and reduce fractionation factors (Verney-Carron and others, 2015;
 891 Pogge von Strandmann and others, 2016). If relative contributions of geothermal waters are
 892 highest in low weathering intensity regimes, for example due to active tectonic uplift
 893 (Chamberlain and others, 2002), this could result in the parabolic $\delta^7\text{Li}_{\text{diss}}$ patterns of figure 7(e–
 894 f): (1) At high weathering intensity, clay dissolution results in low $[\text{Li}^+]$ and low $\delta^7\text{Li}_{\text{diss}}$; (2) at
 895 moderate weathering intensity, where geothermal waters do not contribute significantly to solute
 896 fluxes, primary mineral dissolution coupled with secondary mineral precipitation results in

897 moderate $[\text{Li}^+]$ and high $\delta^7\text{Li}_{\text{diss}}$; and (3) at low weathering intensity, where geothermal waters
 898 contribute significantly to solute fluxes, the inhibition of secondary mineral precipitation during
 899 high temperature weathering results in high $[\text{Li}^+]$ and low $\delta^7\text{Li}_{\text{diss}}$. Geothermal water
 900 contributions in rapidly uplifting collisional orogens have been shown, for example, to control
 901 radiogenic Sr budgets and overall solute fluxes in Himalayan rivers (Evans and others, 2001). As
 902 with our chlorite hypothesis, this mechanism is consistent with riverine observations, and it is
 903 supported by observations of geothermal waters; however, this has not been systematically
 904 evaluated across WI gradients. Future studies targeting the potential role of geothermal waters
 905 and evaluating these competing hypotheses may shed important light on the mechanistic
 906 relationships between weathering environments and Li systematics. In particular, future studies
 907 are needed that target low WI environments including the detailed characterization of weathering
 908 zone mineralogy (for example, the presence of soluble Li-rich minerals, mineralogical P_{Li} values
 909 for secondary phases, and fluid travel times).

911 *Limitations of Approach*

913 One primary limitation of our methodology is that the partition coefficient P_{Li} is set via
 914 mineral stoichiometries rather than evolving as a function of fluid chemistry. Mechanisms for the
 915 latter may include: competing clay phases, recrystallization/Ostwald ripening, sorption-
 916 desorption, and concentration-dependent trace element incorporation. In modeling Li uptake
 917 during clay formation, we chose a simplistic representation of halloysite Li-uptake such that
 918 mineral solubility was only dependent on Si and Al concentrations rather than base cation
 919 concentrations. This allows us to systematically vary P_{Li} across the full 0 to 1 range through
 920 specific trace Li concentration without inducing time- or depth-dependent changes in P_{Li} within
 921 individual simulations. However, it also limits the ability to forward-model or predict $\delta^7\text{Li}$
 922 behavior at a specific site without local constraints on bedrock and secondary phase lithium
 923 concentrations. In particular, it will require extensive field characterization in order to accurately
 924 simulate the effects of evolving clay stability on Li isotope dynamics. Similarly, we do not
 925 include any dependence of instantaneous P_{Li} on $[\text{Li}^+]$, as has been noted experimentally
 926 (Decarreau and others, 2012) and included in other reactive transport frameworks (Wanner and
 927 others, 2014; Bohlin and Bickle, 2019). The incorporation of these dynamics would not change

928 the relationship between f_{Li} and δ^7Li_{diss} at steady-state (fig. 3b, filled circles) but would change
929 the approach to steady state (fig. 3b, colored lines). Additionally, P_{Li} dependence on $[Li^+]$ may
930 extend the reaction timescales over which δ^7Li_{diss} increases. While this may allow for more
931 realistic fluid travel times to support δ^7Li_{diss} observations in low WI environments, it would still
932 result in low $[Li^+]$, in conflict with observations.

933 Catchments are also complex 3-dimensional systems with variable distributions of fluid
934 travel times. As such, rivers may integrate a wide range of flow paths with different f_{Li} and
935 resulting δ^7Li_{diss} , even in the absence of appreciable floodplain exchange. In addition, local
936 heterogeneity may impact the efficiency of reactions relative to that shown here for initially
937 homogeneous domains (Pandey and others, Jung and Navarre-Sitchler, 2018). In spite of the
938 large- and small-scale heterogeneities that exist in catchment and regolith profiles, respectively,
939 the general trends presented in the 1-D simulations here are still applicable (Maher, 2011;
940 Pandey and others, Jung and Navarre-Sitchler, 2018). Thus, although the simulations do not
941 capture full complexity of catchments and initial conditions, they do represent a broad spectrum
942 of flow rates, erosion rates and weathering rates and thus provide general insights into potential
943 behavior of Li isotopes.

944

945

CONCLUSIONS

946

947 In order to probe the relationships between weathering intensity and Li isotope
948 systematics, we incorporate Li isotope fractionation processes into CrunchFlow reactive
949 transport simulations of weathering granite. Using a parsimonious effective kinetic fractionation
950 parameterization, our simulations capture broad patterns in observed relationships between
951 δ^7Li_{diss} and the fraction of dissolved Li remaining in solution following secondary mineral
952 precipitation. Upland weathering profiles are simulated across a range of weathering intensities
953 by varying water infiltration and bedrock uplift/erosion rates. Simulations produce a parabolic
954 relationship between δ^7Li_{diss} and weathering intensity similar to global observations, controlled
955 by a combination of fluid travel times and mineral residence times in the weathering zone.
956 However, fluid travel and mineral residence time controls alone are unable to capture high
957 observed Li concentrations under low weathering intensity conditions: short fluid travel times
958 that limit clay precipitation also limit primary mineral dissolution and solute accumulation.

959 Instead, we demonstrate how mineral residence times may regulate the dominant Li weathering
960 reactions, where the weathering of soluble, Li-rich minerals may only be sustained with the rapid
961 supply of fresh bedrock. This mineralogic control on Li isotope systematics is able to capture
962 parabolic relationships between $\delta^7\text{Li}_{\text{diss}}$ and both weathering intensity and Li concentrations. We
963 suggest that as a viable hypothesis, this mineralogic control may be tested against other possible
964 mechanistic ties between weathering regimes and Li systematics such as varying contributions
965 from geothermal waters.

966 The refinement of a theoretical framework for Li isotope systematics may provide for
967 more accurate reconstructions of weathering dynamics in the past. In particular, direct links
968 between Li-specific congruence (P_{Li}) and overall weathering congruence need to be established
969 in order for Li isotopes to serve as a direct proxy of weathering intensity. Additionally, based on
970 the parabolic relationships described above, tectonic uplift and attendant shifts in weathering
971 may be result in either increasing or decreasing $\delta^7\text{Li}_{\text{diss}}$ values depending on the background
972 weathering intensity. Thus, understanding the mechanistic connections between uplift and $\delta^7\text{Li}_{\text{diss}}$
973 may allow for more direct hypothesis evaluation, for example, through comparisons of proxy
974 $\delta^7\text{Li}$ with coeval records of hydrologic shifts or changes in depositional environment mineralogy
975 along active orogens that may indicate changes in fluid and mineral residence times.

976 977 ACKNOWLEDGEMENTS 978

979 We thank Daniel Ibarra and Jeremy Caves for useful comments and conversations, along with
980 the Friedhelm von Blanckenburg (Associate Editor) and two anonymous reviewers whose
981 comments and suggestions improved an earlier version of this manuscript. This work was
982 supported by the National Science Foundation (EAR-1254156) to K.M. The authors will make
983 updated CrunchFlow software source code and all input files used in this analysis available on
984 request.

985 986 APPENDIX 987

988 *Appendix A: Weathering Reaction Sensitivity Analysis* 989

990 To demonstrate the sensitivity of the presented simulations to assumptions of prescribed P_{Li}
991 values in Figure 8 and to our idealized reaction network, we present analyses showing:
992

- 993 A1) How $\delta^7\text{Li}_{\text{diss}}$ varies as a function of weathering intensity and $[\text{Li}]$ for a range of P_{Li}
994 values, and
- 995 A2) How the use of a 2:1 clay rather than 1:1 halloysite does not impact apparent
996 fractionations.

997
 998 *A.1*—To show the sensitivity of $\delta^7\text{Li}_{\text{diss}}$ to weathering intensity and [Li], we present an altered
 999 version of Figure 7e,f in which simulations are color-coded by prescribed P_{Li} (0.08, 0.53, and
 1000 0.99). As P_{Li} primarily impacts the maximum extent of $\delta^7\text{Li}_{\text{diss}}$ increase during incongruent
 1001 plagioclase weathering, the effect of lowering P_{Li} is to flatten the parabolic curves of $\delta^7\text{Li}_{\text{diss}}$ v.
 1002 WI and $\delta^7\text{Li}_{\text{diss}}$ v. [Li]. In other words, smaller P_{Li} values result in lower ranges of $\delta^7\text{Li}_{\text{diss}}$
 1003 variability. Additionally, P_{Li} values impact the concentrations of Li during incongruent and clay
 1004 weathering along with $\delta^7\text{Li}_{\text{clay}}$ values. This results in variable $\delta^7\text{Li}_{\text{diss}}$ at high weathering intensity
 1005 when clay dissolution dominates and $\delta^7\text{Li}_{\text{diss}}$ matches $\delta^7\text{Li}_{\text{clay}}$ (figure A1a). It also results in [Li⁺]
 1006 variability under both clay dissolution and incongruent weathering: as P_{Li} approaches 1, the
 1007 difference in [Li⁺] under clay dissolution v. incongruent weathering decreases, causing a steeper
 1008 left side of the parabolic curve in figure A1b.

1009
 1010 *A.2*—To demonstrate the insensitivity of our model simulations to alternative representations of
 1011 clay mineralogy, we include batch reactor simulations similar to those presented in the main text
 1012 where halloysite is replaced with a calcium beidellite (2:1 smectite group clay). Kinetic
 1013 fractionation is implemented in the same manner, and we simulate a range of P_{Li} (0.08 – 0.93)
 1014 values based on prescribed substitution of Li⁺ for Ca²⁺ as shown in table A1. We chose to
 1015 simulate a calcium rather than iron or magnesium 2:1 clay based on the lack of magnesium and
 1016 iron in our primary mineral dissolution reaction (Plagioclase An₂₀). Selected results
 1017 corresponding to main text figures 2a,b,d and 3a are shown in figure A2. In comparison to our
 1018 halloysite reaction, the simulation of beidellite alters the patterns of primary mineral dissolution
 1019 and secondary mineral precipitation rates along with the steady-state weathering incongruence
 1020 value representing stoichiometric balance of plagioclase dissolution and beidellite precipitation.
 1021 Changes in the balance of rates are largely related to changes in reaction affinity as kinetic rate
 1022 constants are unchanged from halloysite simulations. Weathering incongruence reflects
 1023 represents the aluminum-normalized stoichiometry. As shown in figure A2, the evolution of
 1024 $\delta^7\text{Li}_{\text{diss}}$ is identical to halloysite both as a function of time and of prescribed P_{Li} . Even though the
 1025 model is simulating a different mechanisms of Li substitution (that is, for substituted cations
 1026 rather than structural aluminum), the P_{Li} value and kinetic fractionation factor together set $\delta^7\text{Li}_{\text{diss}}$
 1027 in the same manner as with structural substitution for Al in halloysite.

1028 *Appendix B: Theoretical Concentration-Discharge Dynamics*

1029
 1030
 1031 In order to explore potential concentration-discharge dynamics encapsulated in our model
 1032 simulations, we convolve idealized watershed travel time distributions with time-varying output
 1033 from main text batch reactor simulations. Numerous studies have shown that times of high flow,
 1034 either in response to transient infiltration events such as storms and snowmelt or sustained
 1035 seasonal changes in precipitation, are associated with relatively lower mean travel times. To
 1036 show how this may be manifested in stream solute data, we assume watershed travel time
 1037 distributions may be represented by a gamma-type distribution as,

1038
 1039
$$h(\tau) = \frac{\tau^{\alpha-1}}{\left(\frac{\tau_m}{\alpha}\right)^\alpha \Gamma(\alpha)} e^{-\tau\alpha/\tau_m},$$

1040

1041 where h is a weight for a given travel time τ , α represents a shape factor, and τ_m is the mean
1042 travel time (for example, Kirchner, 2016).

1043
1044 For the purposes of this exercise, we assume a shape factor of 1. We convolve travel time
1045 distributions with batch reactor experiment $\delta^7\text{Li}_{\text{diss}}$ for a range of mean travel time values by
1046 taking the weighted mean of Li concentration-weighted, time-dependent $\delta^7\text{Li}_{\text{diss}}$ values using
1047 $h(\tau)*[\text{Li}](\tau)$ as the weights. Figure B1 shows how the convolved $\delta^7\text{Li}_{\text{diss}}$ varies in response to
1048 mean travel times. As mean travel time decreases, the associated $\delta^7\text{Li}_{\text{diss}}$ decreases as well. This
1049 relationship is muted relative to the time v. $\delta^7\text{Li}_{\text{diss}}$ curves shown in Figure 3, due to the mixing
1050 across a wide range of travel times as discussed for solutes (for example, Maher, 2011) and
1051 stable isotope ratios (Druhan & Maher, 2017) in previous papers. The largest changes are seen
1052 when mean travel times are in the vicinity of 1 to 3 months corresponding roughly to timescales
1053 of stoichiometric steady-state in the plagioclase dissolution – halloysite precipitation reaction
1054 series. Under these idealized scenarios, an increase in flow resulting in a reduction in mean travel
1055 time would cause a subsequent decrease in $\delta^7\text{Li}_{\text{diss}}$ values, consistent with field observations from
1056 a number of studies. Importantly, while the magnitude of $\delta^7\text{Li}_{\text{diss}}$ change is dependent on the shift
1057 and absolute value of mean travel time between low and high flow along with the shape factor,
1058 the direction of change is not. The precise relationship between mean travel time and discharge is
1059 not well characterized; however, interfacing this stable isotope reactive transport model with
1060 hillslope or watershed hydrologic models may facilitate concentration-discharge relationship
1061 predictions.

1062 REFERENCES

- 1063 Anghel, I., Turin, H. J., Reimus, P. W., 2002, Lithium sorption to Yucca Mountain tuffs: Applied
1064 Geochemistry, v. 17, p. 819-824.
- 1065 Arnorsson, S., Stefansson, A., 1999, Assessment of feldspar solubility constants in water
1066 in the range 0 degrees to 350 degrees C at vapor saturation pressures: American Journal of
1067 Science v. 299, p. 173–209.
- 1068 Bagard, M.-L., West, J. A., Newman, K., Basu, A. R., 2015, Lithium isotope fractionation in the
1069 Ganges-Brahmaputra floodplain and implications for groundwater impact on seawater isotopic
1070 composition: Earth and Planetary Science Letters, v. 432, p. 404-414.
- 1071 Bernal, N. F., Gleeson, S. A., Dean, A. S., Liu, X. M., Hoskin, P., 2014, The source of halogens
1072 in geothermal fluids from the Taupo Volcanic Zone, North Island, New Zealand: Geochimica et
1073 Cosmochimica Acta, v. 126, p. 265-283.
- 1074 von Blanckenburg, F., Hewawasam, T., Kubik, P. W., 2004, Cosmogenic nuclide evidence for
1075 low weathering and denudation in the wet, tropical highlands of Sri Lanka: Journal of
1076 Geophysical Research: Earth Surface, v. 109, F03008, 22 pp.
- 1077 Bohlin, M. S. and Bickle, M. J., 2019, The reactive transport of Li as a monitor of weathering
1078 processes in kinetically limited weathering regimes: Earth and Planetary Science Letters, v. 511,
1079 p. 233-243.

- 1087
1088 Bouchez, J., von Blanckenburg, F., Schuessler, J. A., 2013, Modeling novel stable isotope ratios
1089 in the weathering zone: *American Journal of Science*, v. 313, p. 267-308.
1090
1091 Caves-Rugenstein, J. K., Ibarra, D. E., von Blanckenburg, F., 2019, Neogene cooling driven by
1092 land surface reactivity rather than increased weathering fluxes: *Nature*, v. 571, p. 99-102.
1093
1094 Chamberlain, C. P., Koons, P. O., Meltzer, A. S., Park, S. K., Craw, D., Zeitler, P., and Poage,
1095 M. A., 2002, Overview of hydrothermal activity associated with active orogenesis and
1096 metamorphism: Nanga Parbat, Pakistan Himalaya: *American Journal of Science*, v. 302(8), p.
1097 726-748.
1098
1099 Chamberlain, C. P., Waldbauer, J. R., Jacobson, A. D., 2005, Strontium, hydrothermal systems
1100 and steady-state chemical weathering in active mountain belts: *Earth and Planetary Science*
1101 *Letters*, v. 238, p. 351-366.
1102
1103 Chan, L. H., Edmond, J. M., Thompson, G., Gillis, K., 1992, Lithium isotopic composition of
1104 submarine basalts: implications for the lithium cycle in the oceans: *Earth and Planetary Science*
1105 *Letters*, v. 108, p. 151-160.
1106
1107 Decarreau, A., Vigier, N., Pálková, H., Petit, S., Vieillard, P., Fontaine, C., 2012, Partitioning of
1108 lithium between smectite and solution: An experimental approach: *Geochimica et Cosmochimica*
1109 *Acta*, v. 85, p. 314-325.
1110
1111 Dellinger, M., Gaillardet, J., Bouchez, J., Calmels, D., Galy, V., Hilton, R. G., Louvat, P.,
1112 France-Lanord, C., 2014, Lithium isotopes in large rivers reveal the cannibalistic nature of
1113 modern continental weathering and erosion: *Earth and Planetary Science Letters*, v. 401, p. 359-
1114 372.
1115
1116 Dellinger, M., Gaillardet, J., Bouchez, J., Calmels, D., Louvat, P., Dosseto, A., Gorge, C.,
1117 Alanoca, L., Maurice, L., 2015, Riverine Li isotope fractionation in the Amazon River basin
1118 controlled by the weathering regimes: *Geochimica et Cosmochimica Acta*, v. 164, p. 71-93.
1119
1120 Dellinger, M., Bouchez, J., Gaillardet, J., Faure, L., Moureau, J., 2017, Tracing weathering
1121 regimes using the lithium isotope composition of detrital sediments: *Geology*, v. 45, p. 411-414.
1122
1123 Druhan, J. L., Steefel, C. I., Williams, K. H., DePaolo, D. J., 2013, Calcium isotope fractionation
1124 in groundwater: Molecular scale processes influencing field scale behavior: *Geochimica et*
1125 *Cosmochimica Acta*, v. 119, p. 93-116.
1126
1127 Druhan, J. L., and Maher, K., 2017, The influence of mixing on stable isotope ratios in porous
1128 media: A revised Rayleigh model: *Water Resources Research*, v. 53(2), p. 1101-1124.
1129
1130 Druhan, J. L., and Winnick, M. J., 2019, Reactive transport of stable isotopes: *Elements*, v.
1131 15(2), p. 107-110.
1132

- 1133 Evans, M. J., Derry, L. A., Anderson, S. P., France-Lanord, C., 2001, Hydrothermal source of
1134 radiogenic Sr to Himalayan rivers: *Geology*, v. 29(9), p. 803-806.
1135
- 1136 Ferrier, K. L., Kirchner, J. W., 2008, Effects of physical erosion on chemical denudation rates: A
1137 numerical modeling study of soil-mantled hillslopes: *Earth and Planetary Science Letters*, v. 272,
1138 p. 591-599.
1139
- 1140 Flesch, G. D., Anderson Jr., A. R., Svec, H. J., 1973, A secondary isotopic standard for $^6\text{Li}/^7\text{Li}$
1141 determinations: *International Journal of Mass Spectrometry Ion Physics*, v. 12(3), p. 2655-272.
1142
- 1143 Gibbs, R. J., 1967, The geochemistry of the Amazon River system: Part I. The factors that
1144 control the salinity and the composition and concentration of the suspended solids: *Geological*
1145 *Society of America Bulletin*, v. 78, p. 1203-1232.
1146
- 1147 Godfrey, L., Álvarez-Amado, F., 2020, Volcanic and saline lithium inputs to the Salar de
1148 Atacam: *Minerals*, v. 10, pp. 17.
1149
- 1150 Golla, J. K., Kuessner, M. L., Henehan, M. J., Bouchez, J., Rempe, D. M., & Druhan, J. L., 2021,
1151 The evolution of lithium isotope signatures in fluids draining actively weathering
1152 hillslopes: *Earth and Planetary Science Letters*, v. 567, p. 116988.
1153
- 1154 Gu, X., Rempe, D. M., Dietrich, W. E., West, A. J., Lin, T.-C., Jin, L., Brantley, S. L., 2020,
1155 Chemical reactions, porosity, and microfracturing in shale during weathering: The effect of
1156 erosion rate: *Geochimica et Cosmochimica Acta*, v. 269, p. 63-100.
1157
- 1158 Heidari, P., Li, L., Jin, L., Williams, J. Z., Brantley, S. L., 2017, A reactive transport model for
1159 Marcellus shale weathering: *Geochimica et Cosmochimica Acta*, v. 217, p. 421-440.
1160
- 1161 Hindshaw, R. S., Tosca, R., Goût, T. L., Farnan, I., Tosca, N. J., Tipper, E. T., 2019,
1162 Experimental constraints on Li isotope fractionation during clay formation. *Geochimica et*
1163 *Cosmochimica Acta*, v. 250, p. 219-237.
1164
- 1165 Holland H., 1984, The chemical evolution of the atmosphere and oceans: Princeton University
1166 Press.
1167
- 1168 Huh, Y., Chan, L.-H., Edmond, J. M., 2001, Lithium isotopes as a probe of weathering
1169 processes: Orinoco River: *Earth and Planetary Science Letters*, v. 194, p. 189-199.
1170
- 1171 Irion, G., 1983, Clay mineralogy of the suspended load of the Amazon and of rivers in the
1172 Papua-New Guinea mainland: *Mitteilungen Geologie und Palaontologie Institut Universität*
1173 *Hamburg*, v. 55, p. 483-504.
1174
- 1175 Jasechko, S., Kirchner, J. W., Welker, J. M., McDonnell, J. J., 2016, Substantial proportion of
1176 global streamflow less than three months old: *Nature Geoscience*, v. 9, p. 126-129.
1177

- 1178 Jin, L., Ravella, R., Ketchum, B., Bierman, P. R., Heaney, P., White, T., Brantley, S. L., 2010,
1179 Mineral weathering and elemental transport during hillslope evolution at the Susquehanna/Shale
1180 Hills Critical Zone Observatory: *Geochimica et Cosmochimica Acta*, v. 74(13), p. 3669-3691.
1181
- 1182 Jung, H. and Navarre-Sitchler, A., 2018, Physical heterogeneity control on effective mineral
1183 dissolution rates: *Geochimica et Cosmochimica Acta*, v. 227, p. 246-263.
1184
- 1185 Kirchner, J.W., 2016, Aggregation in environmental systems – Part 1: Seasonal tracer cycles
1186 quantify young water fractions, but not mean transit times, in spatially heterogeneous
1187 catchments: *Hydrology and Earth System Sciences*, v. 20, p. 279-297.
1188
- 1189 Lara, M.C., Buss, H., Henehan, M.J., Schuessler, J.A., McDowell, W.H., 2022, Secondary
1190 minerals drive extreme lithium isotope fractionation during tropical weathering: *JGR Earth
1191 Surface*, v. 127, e2021JF006366.
1192
- 1193 Lasaga, A.C., 1998, *Kinetic theory in the earth sciences*: v. 811. Princeton, NJ: Princeton
1194 university press, 1998.
1195
- 1196 Lebedeva, M. I., Fletcher, R. C., Brantley, S. L., 2010, A mathematical model for steady-state
1197 regolith production at constant erosion rate: *Earth Surface Processes and Landforms*, v. 35, p.
1198 508-524.
1199
- 1200 Lebedeva, M. I. and Brantley, S. L., 2013, Exploring geochemical controls on weathering and
1201 erosion of convex hillslopes: beyond the empirical regolith production function: *Earth Surface
1202 Processes and Landforms*, v. 38(15), p. 1793-1807.
1203
- 1204 Lechler, M., Pogge von Strandmann, P. A. E., Jenkyns, H. C., Prosser, G., Parente, M., 2015,
1205 Lithium-isotope evidence for enhanced silicate weathering during OAE 1a ,Early Aptian Selli
1206 event: *Earth and Planetary Science Letters*, v. 432, p. 210-222.
1207
- 1208 Lemarchand, E., Chabaux, R., Vigier, N., Millot, R., Pierret, M.-C., 2010, Lithium isotope
1209 systematics in a forested granitic catchment, Strengbach, Vosges Mountains, France:
1210 *Geochimica et Cosmochimica Acta*, v. 74(16), p. 4612-4628.
1211
- 1212 Li, G. and West, J. A., 2014, Evolution of Cenozoic seawater lithium isotopes: Coupling of
1213 global denudation regime and shifting seawater sinks: *Earth and Planetary Science Letters*, v.
1214 401, p. 284-293.
1215
- 1216 Lawson, R. T., Comarmond, M.-C. J., Rajaratnam, G., Brown, P. L., 2005, The kinetics of the
1217 dissolution of chlorite as a function of pH and at 25°C: *Geochimica et Cosmochimica Acta*, v.
1218 69(7), p. 1687-1699.
1219
- 1220 Maffre, P., Godderis, Y., Vigier, N., Moquet, J.-S., Carretier, S., 2020, Modelling the riverine
1221 $\delta^7\text{Li}$ variability throughout the Amazon Basin: *Chemical Geology*, v. 532, 119336.
1222

- 1223 Maher, K., Steefel, C. I., DePaolo, D. J., & Viani, B. E., 2006, The mineral dissolution rate
1224 conundrum: Insights from reactive transport modeling of U isotopes and pore fluid chemistry in
1225 marine sediments: *Geochimica et Cosmochimica Acta*, v. 70(2), p. 337-363.
1226
- 1227 Maher, K., 2010, The dependence of chemical weathering rates on fluid residence time: *Earth
1228 and Planetary Science Letters*, v. 294, p. 101-110.
1229
- 1230 Maher, K., 2011, The role of fluid residence time and topographic scales in determining
1231 chemical fluxes from landscapes: *Earth and Planetary Sciences*, v. 312, p. 48-58.
1232
- 1233 Maher, K., Chamberlain, C. P., 2014, Hydrologic regulation of chemical weathering and the
1234 geologic carbon cycle: *Science*, v. 343, p. 1502-1504.
1235
- 1236 Maher, K., von Blanckenburg, F., 2016, Surface ages and weathering rates from ^{10}Be , meteoric,
1237 and $^{10}\text{Be}/^9\text{Be}$: Insights from differential mass balance and reactive transport modeling: *Chemical
1238 Geology*, v. 446, p. 70-86.
1239
- 1240 Manaka, T., Araoka, D., Yoshimura, T., Hossain, H. M. Z., Nishio, Y., Suzuki, A., Kawahata,
1241 H., 2017, Downstream and seasonal changes of lithium isotope ratios in the Ganges-
1242 Brahmaputra river system: *Geochemistry, Geophysics, Geosystems*, v. 18(8), p. 3003-3015.
1243
- 1244 Maxwell, R. M., Condon, L. E., Kollet, S. J., Maher, K., Haggerty, R., Forrester, M. M., 2015,
1245 The imprint of climate and geology on the residence times of groundwater: *Geophysical
1246 Research Letters*, v. 43(2), p. 701-708.
1247
- 1248 Millot, R., Girard, J. P., 2007, Lithium isotope fractionation during adsorption onto mineral
1249 surfaces: *Clay in Natural and Engineered Barriers for Radioactive Waste Confinement*, 3rd
1250 International Meeting – Lille.
1251
- 1252 Millot, R., Negrel, P., 2007, Multi-isotopic tracing $\delta^7\text{Li}$, $\delta^{11}\text{B}$, $^{87}\text{Sr}/^{86}\text{Sr}$, and chemical
1253 geothermometry: evidence from hydro-geothermal systems in France: *Chemical Geology*, v.
1254 244, p. 664-678.
1255
- 1256 Millot, R., Negrel, P., Petelet-Giraud, E., 2007, Multi-isotopic Li, B, Sr, Nd, approach for
1257 geothermal reservoir characterization in the Limagne Basin, Massif Central, France: *Applied
1258 Geochemistry*, v. 22, p. 2307-2335.
1259
- 1260 Millot, R., Vigier, N., Gaillardet, J., 2010a, Behavior of lithium and its isotopes during
1261 weathering in the Mackenzie Basin, Canada: *Geochimica et Cosmochimica Acta*, v. 74, p. 3897-
1262 3912.
1263
- 1264 Millot, R., Scaillet, B., Sanjuan, B., 2010b, Lithium isotopes in arc geothermal systems:
1265 Guadeloupe, Martinique, French West Indies, and experimental approach: *Geochimica et
1266 Cosmochimica Acta*, v. 74, p. 1852-1871.
1267

- 1268 Millot, R., Hegan, A., Negrel P., 2012, Geothermal waters from the Taupo Volcanic Zone, New
1269 Zealand: Li, B, and Sr isotopes characterization: Applications in Geochemistry, v. 27, p. 677-
1270 688.
- 1271
1272 Misra, S., Froelich, P. N., 2012, Lithium isotope history of Cenozoic seawater: changes in
1273 silicate weathering and reverse weathering: Science, v. 335, p. 818-823.
- 1274
1275 Murphy, S. F., Brantley, S. L., Blum, A. E., White, A. F., Dong, H., 1998, Chemical weathering
1276 in a tropical watershed, Luquillo Mountains, Puerto Rico: II. Rate and mechanism of biotite
1277 weathering: *Geochimica et Cosmochimica Acta*, v. 62(2), p. 227-243.
- 1278
1279 Palandri, J. L. and Kharaka, Y. K., 2004, A compilation of rate parameters of water–mineral
1280 interaction kinetics for application to geochemical modeling Rep. 2004–1068: US
1281 Geological Survey Open File Report.
- 1282
1283 Pandey, S. and Rajaram, H., 2016, Modeling the influence of preferential flow on the spatial
1284 variability and time-dependence of mineral weathering rates: *Water Resources Research*, v.
1285 52(12), p. 9344-9366.
- 1286
1287 Penniston-Dorland, S., Liu, X.-M., Rudnick, R. L., 2017, Lithium Isotope Geochemistry:
1288 Reviews in Mineralogy and Geochemistry, v. 82, p. 165-217.
- 1289
1290 Perez-Fodich, A., Derry, L.A., 2020, A model for germanium-silicon equilibrium fractionation in
1291 kaolinite: *Geochimica et Cosmochimica Acta*, v. 288, p. 199-213.
- 1292
1293 Pistiner, J. S., and Henderson, G. M., 2003, Lithium-isotope fractionation during continental
1294 weathering process: *Earth and Planetary Science Letters*, v. 214, n. 1–2, p. 327–339.
- 1295
1296 Pogge von Strandmann, P. A. E., Henderson, G. M., 2015, The Li isotope response to mountain
1297 uplift: *Geology*, v. 43, p. 67-70.
- 1298
1299 Pogge von Strandmann, P. A. E., Jenkyns, H. C., Woodfine, R. G., 2013, Lithium isotope
1300 evidence for enhanced weathering during Oceanic Anoxic Event 2: *Nature Geoscience*, v. 6, p.
1301 668-672.
- 1302
1303 Pogge von Strandmann, P. A. E, Burton, K. W., Opfergelt, S., Eiriksdottir, E. S., Murphy, M. J.,
1304 Einarsson, A., Gislason, S. R., 2016, The effect of hydrothermal spring weathering processes and
1305 primary productivity on lithium isotopes: *Lake Myvatn, Iceland: Chemical Geology*, v. 445, p. 4-
1306 13.
- 1307
1308 Pogge von Strandmann, P. A. E., Desrochers, A., Murphy, M. J., Finlay, A. J., Selby, D., Lenton,
1309 T. M., 2017, Global climate stabilisation by chemical weathering during the Hirnantian
1310 glaciation: *Geochemical Perspectives Letters*, v. 3, p. 230-237.
- 1311
1312 Pogge von Strandmann, P. A. E., Kasemann, S. A., Wimpenny, J. B., 2020, Lithium and lithium
1313 isotopes in Earth's surface cycles: *Elements*, v. 16(4), p. 253-258.

- 1314
1315 Proust, D., Eymery, J.-P., Beaufort, D., 1986, Supergene vermiculitization of a magnesian
1316 chlorite: Iron and magnesium removal processes: *Clays and Clay Minerals*, v. 34, p. 572-580.
1317
1318 Steefel, C. I., C. A. J. Appelo, B. Arora, D. Jacques, T. Kalbacher, O. Kolditz, V. Lagneau, P. C.
1319 Lichtner, K. U. Mayer, J. C. L. Meeussen, S. Molins, D. Moulton, H. Shao, J. Simunek, N.
1320 Spycher, S. B. Yabusaki and G. T. Yeh, 2015, Reactive transport codes for subsurface
1321 environmental simulation: *Computational Geosciences*, v. 19(3), p. 445-478.
1322
1323 Sullivan, P. L., Hynek, S. A., Gu, X., Singha, K., White, T., West, N., Kim, H., Clarke, B.,
1324 Kirby, E., Duffy, C., Brantley, S. L., 2016, Oxidative dissolution under the channel leads
1325 geomorphological evolution at the Shale Hills catchment: *American Journal of Science*, v. 316,
1326 p. 981-1026.
1327
1328 Sun, H., Xiao, Y., Gao, Y., Zhang, G., Casey, J. F., Shen, Y., 2018, Rapid enhancement of
1329 chemical weathering recorded by extremely light seawater lithium isotopes at the Permian-
1330 Triassic boundary: *Proceedings of the National Academy of Sciences*, v. 115(15), p. 3782-3787.
1331
1332 Tardy, Y., Krempp, G., Trauth, N., 1972, Le lithium dans les minéraux argileux des sédiments et
1333 des sols: *Geochimica et Cosmochimica Acta*, v. 36, p. 397-412.
1334
1335 Templeton, A. S., Chamberlain, C. P., Koons, P. O., and Craw, D., 1998, Stable isotopic
1336 evidence for mixing between metamorphic fluids and surface-derived waters during recent uplift
1337 of the Southern Alps, New Zealand: *Earth and Planetary Science Letters*, v. 154, p. 73-92.
1338
1339 Teng, F. Z., McDonough, W. F., Rudnick, R. L., Dalpe, C., Tomascak, P. B., Chappell, B. W.,
1340 Gao, S., 2004, Lithium isotopic composition and concentration of the upper continental crust:
1341 *Geochimica et Cosmochimica Acta*, v. 68, p. 4167-4178.
1342
1343 Tomascak, P. B., 2004, Developments in the understanding and application of lithium isotopes in
1344 the earth and planetary sciences in geochemistry of non-traditional stable isotopes: *Reviews in*
1345 *Mineralogy and Geochemistry*, v. 55, p. 153-195.
1346
1347 Verney-Carron, A., Vigier, N., Millot, R., Hardarson, B. S., 2015, Lithium isotopes in
1348 hydrothermally altered basalts from Hengill, SW Iceland: *Earth and Planetary Science Letters*, v.
1349 411, p. 62-71.
1350
1351 Vigier, N., Decarreau, A., Millot, R., Carignan, J., Petit, S., France-Lanord, C., 2008,
1352 Quantifying Li isotope fractionation during smectite formation and implications for the Li cycle:
1353 *Geochimica et Cosmochimica Acta*, v. 72, p. 780-792.
1354
1355 Vigier, N., Gislason, S., Burton, K., Millot, R., Mokadem, F., 2009, The relationship between
1356 riverine lithium isotope composition and silicate weathering rates in Iceland: *Earth and Planetary*
1357 *Science Letters*, v. 287, p. 434-441.
1358

- 1359 Wang, Y., Xu, H., 2001, Prediction of trace metal partitioning between minerals and aqueous
1360 solutions: a linear free energy correlation approach: *Geochimica et Cosmochimica Acta*,
1361 v. 65, p. 1529-1543.
1362
- 1363 Wanner, C., Sonnenthal, E. L., Liu, X.-M., 2014, Seawater $\delta^7\text{Li}$: A direct proxy for global CO_2
1364 consumption by continental silicate weathering?: *Chemical Geology*, v. 381, p. 154-167.
1365
- 1366 Williams, L. B., Hervig, R. L., 2005, Lithium and boron isotopes in illite-smectite: the
1367 importance of crystal size: *Geochimica et Cosmochimica Acta*, v. 24, p. 5705-5716.
1368
- 1369 Wimpenny J., Gisalason, S. R., James, R. H., Gannoun, A., Pogge von Strandmann, P. A. E.,
1370 Burton, K. W., 2010, The behavior of Li and Mg isotopes during primary phase dissolution and
1371 secondary mineral formation in basalt: *Geochimica et Cosmochimica Acta*, v. 74, 5259-5279.
1372
- 1373 Winnick, M. J., Maher, K., 2018, Relationships between CO_2 , thermodynamic limits on silicate
1374 weathering, and the strength of the silicate weathering feedback: *Earth and Planetary Science*
1375 *Letters*, v. 485, p. 111-120.
1376
- 1377 Wolery, T. J., Jackson, K. J., Bourcier, W. L., Bruton, C. J., Viani, B. E., Knauss, K. G., Delany,
1378 J. M., 1990, Current status of the EQ3/6 software package for geochemical modeling: *ACS*
1379 *Symposium Series*, v. 416, p. 104–116.
1380
- 1381 Zhang, L., Chan, L. H., Gieskes, J. M., 1998, Lithium isotope geochemistry of pore waters from
1382 Ocean Drilling Program Sites 918 and 919, Irminger Basin: *Geochimica et Cosmochimica Acta*
1383 v. 62, p. 2437-2450.
1384
- 1385 Zhang, X., Saldi, G. D., Schott, J., Bouchez, J., Kuessner, M, Montouillout, V., Henehan, M.,
1386 Gailardet, J., 2021, Experimental constraints on Li isotope fractionation during the interaction
1387 between kaolinite and seawater. *Geochimica et Cosmochimica Acta* v. 292, p. 333-347.
1388
- 1389 Zhu, C., 2005, In situ feldspar dissolution rates in an aquifer: *Geochimica et Cosmochimica*
1390 *Acta*, v. 69(6), p. 1435-1453.
1391

FIGURE CAPTIONS

1395 Table 1. CrunchFlow reaction network.

1396
1397 Table 2. Weathering simulation scenarios.

1398
1399 Table 3. Variables calculated from model output.

1400
1401 Figure 1. Conceptual diagram of lithium isotope systematics based on observational and
1402 theoretical studies (Bouchez and others, 2013; Dellinger and others, 2015). The top graph shows
1403 general patterns of $\delta^7\text{Li}_{\text{diss}}$ as a function of weathering intensity (WI), soil residence time, and
1404 dissolved Li concentrations. Points A, B, and C represent medium, high, and low WI,

1405 respectively, and are described in the Introduction. The bottom panel shows relative rates of
 1406 regolith production, physical erosion (E), and chemical weathering (W), with increasing WI (left
 1407 to right), along with depictions of idealized regolith profiles showing the weathering of primary
 1408 minerals (gray) and accumulation of secondary minerals (brown).
 1409

1410 Figure 2. Batch reactor (Scenario 1) results for granitic weathering (no chlorite) showing the
 1411 temporal evolution of (a) plagioclase and halloysite dissolution/precipitation rates; (b)
 1412 weathering incongruence calculated as the ratio of halloysite precipitation to plagioclase
 1413 dissolution rates; (c) dissolved Ca^{2+} concentration representing fully congruent weathering; and
 1414 (d) dissolved Li^+ concentrations across a range of partitioning coefficients (colored lines).
 1415

1416 Figure 3. Lithium isotope behavior in batch reactor experiments. (A) Temporal evolution of
 1417 $\delta^7\text{Li}_{\text{diss}}$ for a range of partition coefficients (as in fig. 2D); (B) $\delta^7\text{Li}_{\text{diss}}$ as a function of fraction Li
 1418 left in solution. Amazon basin data from Dellinger and others (2015) shown in gray, and samples
 1419 interpreted to reflect floodplain uptake processes denoted.
 1420

1421 Figure 4. No Erosion (Scenario 2) CrunchFlow simulations of weathering profiles showing (a)
 1422 plagioclase solid phase (vol. %); (b) halloysite solid phase (vol. %); (c) weathering incongruence
 1423 (ratio of instantaneous halloysite precipitation to plagioclase dissolution rates); (d) dissolved
 1424 $[\text{Ca}^{2+}]$, (e) dissolved $[\text{Li}^+]$, and (d) $\delta^7\text{Li}_{\text{diss}}$. Simulation timesteps are denoted by line color.
 1425 Simulations depicted have a P_{Li} value of 0.9.
 1426

1427 Figure 5. Crunchflow simulations of granitic weathering (Scenario 3) including uplift and
 1428 erosion. Weathering profile results for low (a–e), medium (f–j), and high (k–o) weathering
 1429 intensity conditions. Columns from left to right show solid phase plagioclase, solid phase
 1430 halloysite, weathering incongruence, dissolved $[\text{Li}^+]$, and $\delta^7\text{Li}_{\text{diss}}$. Gray shading denotes un-
 1431 weathered bedrock defined as model cells with $<101\%$ initial porosity. Colored lines denote
 1432 model timestep. Red bars in d, i, and n denote approximate observational ranges of $[\text{Li}^+]$ from
 1433 Dellinger and others (2015) for low, medium, and high weathering intensity, respectively.
 1434 Simulations depicted have a P_{Li} value of 0.9.
 1435

1436 Figure 6. Crunchflow simulations including chlorite (Scenario 4) and vermiculite minerals from
 1437 Table 1. Weathering profile results for low (a–d), medium (e–h), and high (i–l) weathering
 1438 intensity conditions. Columns from left to right show solid phase plagioclase, solid phase
 1439 chlorite, dissolved $[\text{Li}^+]$, and $\delta^7\text{Li}_{\text{diss}}$. Gray shading denotes un-weathered bedrock defined as
 1440 model cells with $<101\%$ initial porosity. Colored lines denote model timestep. Red bars in c, g,
 1441 and k denote approximate observational ranges of $[\text{Li}^+]$ from Dellinger and others (2015) for
 1442 low, medium, and high weathering intensity, respectively. Simulations depicted have a P_{Li} value
 1443 of 0.9.
 1444

1445 Figure 7. Relationships between $\delta^7\text{Li}_{\text{diss}}$ and Weathering Intensity (left) and dissolved Li
 1446 concentrations (right). Results show model output (a–b) without chlorite; (c–d) with chlorite; and
 1447 (e–f) global riverine observations from Dellinger and others (2015) and references therein.
 1448 Simulations depicted have a P_{Li} value of 0.9.
 1449

1450 Figure 8. $\delta^7\text{Li}$ of fine-grained suspended material as a function of weathering intensity for
1451 CrunchFlow simulations (black dots; no chlorite simulations) and observational data from the
1452 Amazon basin (Dellinger and others, 2017). Model output includes the full range of lithium
1453 partition coefficients shown in Figure 3, and CrunchFlow output range is denoted by gray
1454 shading.

1455

1456

APPENDIX FIGURE CAPTIONS

1457

1458 Table A1. CrunchFlow reaction network for plagioclase dissolution – beidellite precipitation
1459 batch reactor sensitivity experiments.

1460

1461 Figure A1. Relationships between $\delta^7\text{Li}_{\text{diss}}$ and Weathering Intensity (left) and dissolved Li
1462 concentrations (right) for erosion/uplift simulations with chlorite across a range of P_{Li} values.

1463

1464 Figure A2. Batch reactor output for plagioclase dissolution and beidellite precipitation showing
1465 (left) mineral precipitation/dissolution rates; (center) weathering congruence; and (right) $\delta^7\text{Li}_{\text{diss}}$
1466 as a function of time for a range of P_{Li} values.

1467

1468 Figure B1. Changes in Li concentrations and $\delta^7\text{Li}_{\text{diss}}$ with mean fluid transit time assuming a
1469 gamma-function transit time distribution with alpha value of 1. The discharge arrow shows
1470 qualitative relationships between discharge and mean transit times and demonstrating negative
1471 C-Q relationships for Li concentrations and $\delta^7\text{Li}_{\text{diss}}$ in simulations.

Table 1. CrunchFlow reaction network.

Mineral	Reaction	log(K _{eq}) @ 298 K	log(k)
Plagioclase (An ₂₀)	$\text{Ca}_{0.2}\text{Na}_{0.79739}{}^7\text{Li}_{0.002409}{}^6\text{Li}_{0.0001948}\text{Al}_{1.2}\text{Si}_{2.8}\text{O}_8 \leftrightarrow 0.2\text{Ca}^{2+} + 0.79739\text{Na}^+ + 0.002409{}^7\text{Li}^+ + 0.0001948{}^6\text{Li}^+$ + 1.2AlO ₂ ⁻ + 2.8SiO ₂ (aq)	-20.076	-14.84
Quartz	SiO ₂ (qz) ↔ SiO ₂ (aq)	-3.9993	-55
Halloysite_7Li	$\text{Al}_{2-0.33x}{}^7\text{Li}_x\text{Si}_2\text{O}_5(\text{OH})_4 + 6\text{H}^+ \leftrightarrow (2-0.33x)\text{AlO}_2^- + x{}^7\text{Li}^+ + 2\text{SiO}_2(\text{aq}) + \text{H}_2\text{O}^*$	-36.4537	-17.14
Halloysite_6Li	$\text{Al}_{2-0.33x}{}^6\text{Li}_x\text{Si}_2\text{O}_5(\text{OH})_4 + 6\text{H}^+ \leftrightarrow (2-0.33x)\text{AlO}_2^- + x{}^6\text{Li}^+ + 2\text{SiO}_2(\text{aq}) + \text{H}_2\text{O}^*$	-36.4537	Precip: -17.13225 Diss: -17.14
Chlorite ^a	$\text{Mg}_{1.03969}{}^7\text{Li}_{0.0005769}{}^6\text{Li}_{0.00004683}\text{Fe}_{0.2}\text{K}_{1.28}\text{Al}_{2.24}\text{Si}_3\text{H}_{13.52}\text{O}_{18} + 10.48\text{H}^+ \leftrightarrow 1.03989\text{Mg}^{2+} + 0.0005769{}^7\text{Li}^+ +$ 0.00004683 ⁶ Li ⁺ + 0.2Fe ²⁺ + 1.28K ⁺ + 2.24Al ³⁺ + 3SiO ₂ (aq) + 12H ₂ O	14.996	-13
Vermiculite ^a	$\text{Mg}_{0.1997}{}^7\text{Li}_{0.000576923}{}^6\text{Li}_{0.00004683}\text{Fe}_{0.441}\text{K}_{1.3}\text{Al}_{4.4}\text{Si}_{1.6}\text{H}_{8.52}\text{O}_{15.2} + 15.5\text{H}^+ \leftrightarrow 0.2\text{Mg}^{2+} + 0.010962{}^7\text{Li}^+ +$ 0.0008897 ⁶ Li ⁺ + 0.3941Fe ²⁺ + 1.3K ⁺ + 4.4Al ³⁺ + 1.6SiO ₂ (aq) + 12H ₂ O	-5.39	-13

* x varies from 0.00035 - 0.0043

^a Based on Heidari et al. (2017)

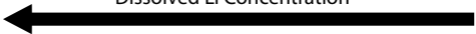
Table 2. Weathering simulation scenarios

Weathering Scenarios	Simulation Length (kyrs)	Infiltration Rate (m/yr)	Uplift/Erosion Rate (mm/yr)	Weathering Intensity
Scenario 1. Batch Reactor	10	NA	NA	NA
Scenario 2. "Chronosequence"	1000	0.5	NA	NA
Scenario 3. Uplift/Erosion	500	0.01 - 5	0.005 - 0.2	0.00045 - 0.927
Scenario 4. Uplift/Erosion w/ Chlorite	500	0.01 - 5	0.005 - 0.2	0.0056 - 0.72

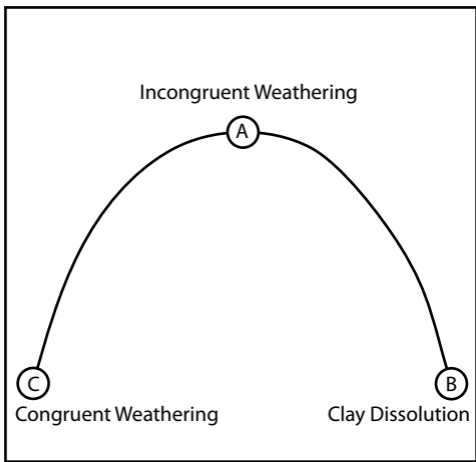
Table 3. Variables calculated from model output

Model Output/Metric	Formula	Description
Erosion Rate (Mass) (t/km ² /yr)	$E = RP*BD$	Prescribed volumetric regolith production (mm/yr) multiplied by bulk density (BD; kg/m ³) in the top model cell
Chemical Denudation Rate (t/km ² /yr)	$W = Q*([Ca^{2+}] + [Mg^{2+}] + [Na^+] + [K^+] + [SiO2_{(aq)}])*1000$	Prescribed infiltration rate (Q; m/yr) multiplied by dissolved solute load (g/L), evaluated at model domain base and weathering zone base
Weathering Intensity	$WI = W/(W + E)$	Ratio of chemical denudation rate to total denudation rate
Suspended Load δ^7Li (‰)	$\delta^7Li_{sus} = (M_{plag} * C_{plag} * \delta^7Li_{plag} + M_{chlor} * C_{chlor} * \delta^7Li_{chlor} + M_{halloy} * C_{halloy} * \delta^7Li_{halloy}) / (M_{plag} * C_{plag} + M_{chlor} * C_{chlor} + M_{halloy} * C_{halloy})$	Lithium mass-weighted δ^7Li composition of non-quartz minerals in the eroding top model cell, where M represents mineral mass and C represents mineral lithium concentration
Weathering Incongruence	$I = -R_{halloysite} / R_{plagioclase}$	Instantaneous ratio of halloysite precipitation to plagioclase dissolution rates

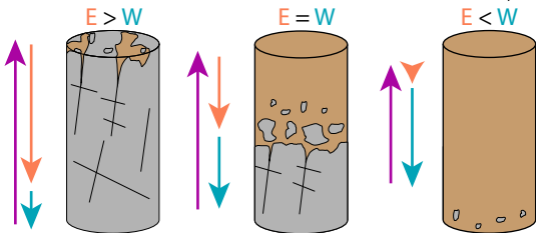
Dissolved Li Concentration



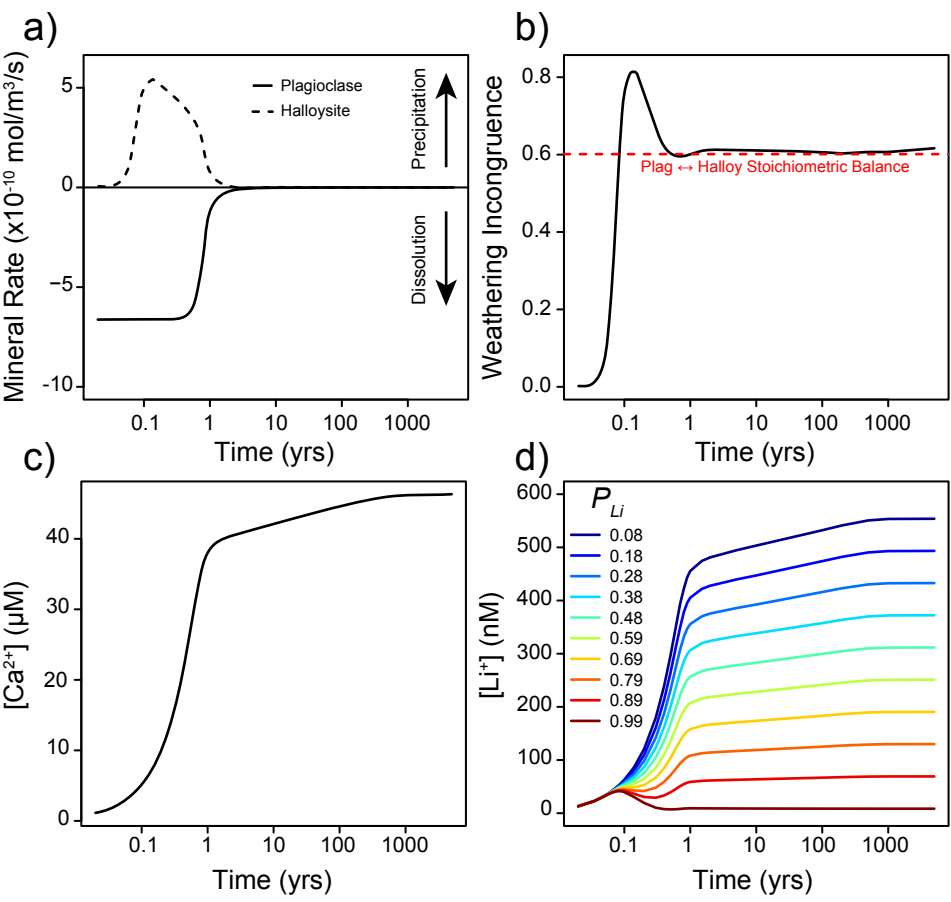
$\delta^7\text{Li}_{\text{Diss}}$ (‰)

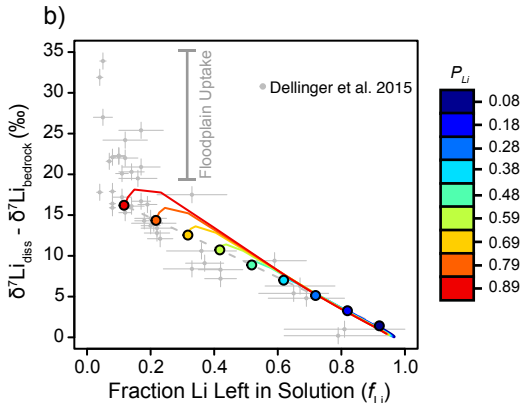
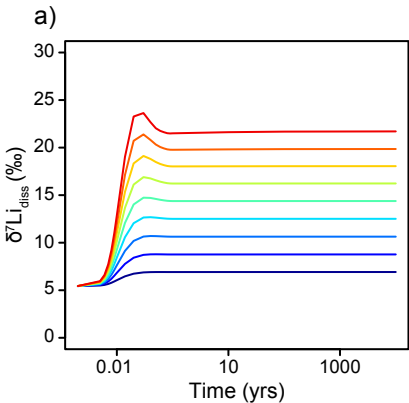


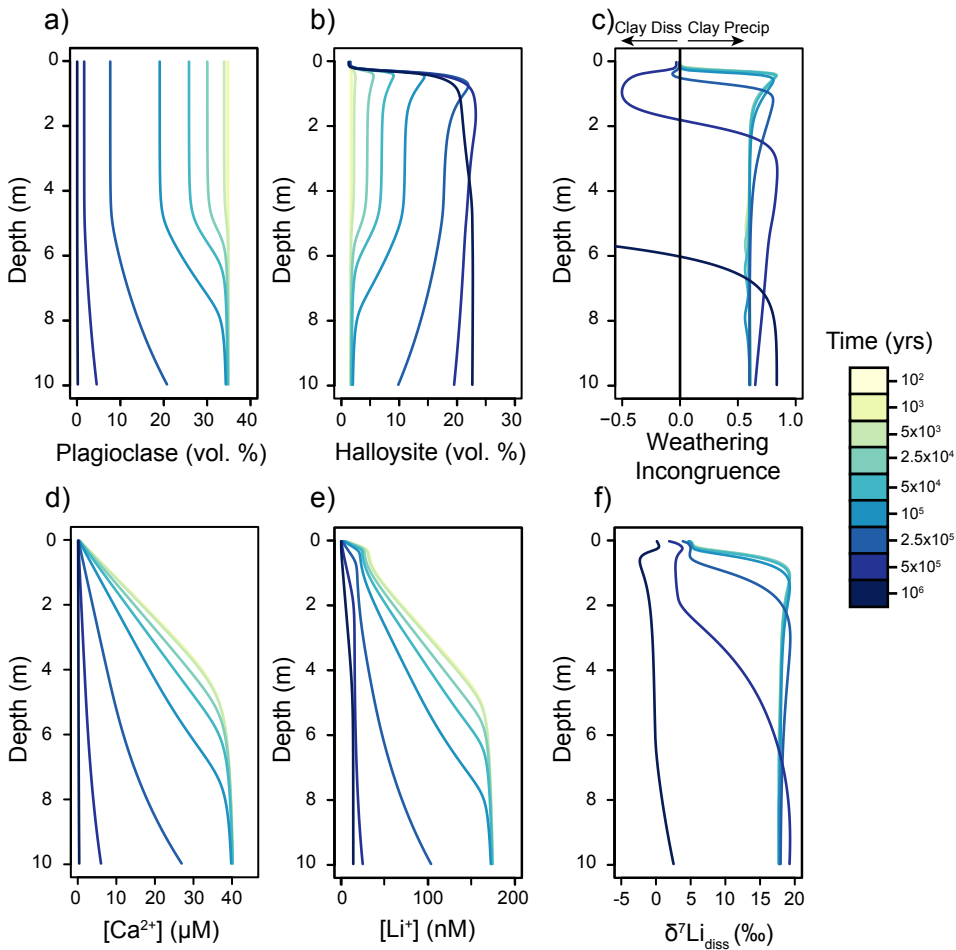
Weathering Intensity & Soil Residence Time

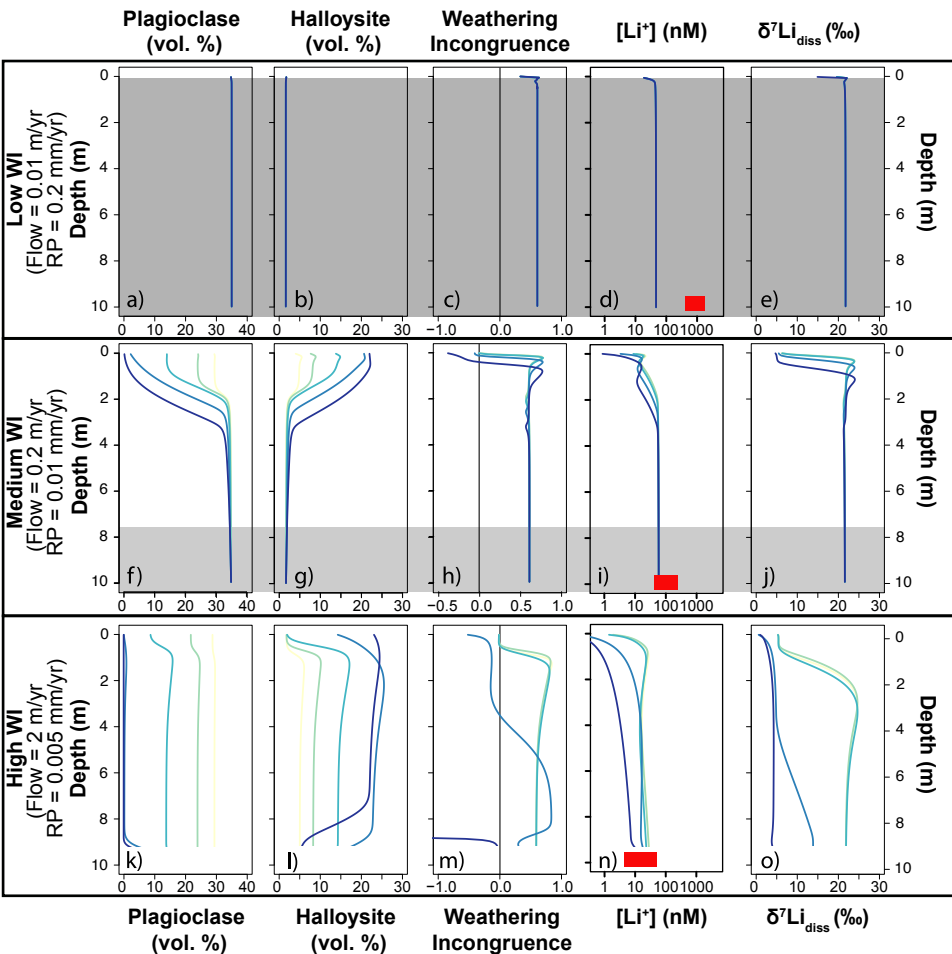


Regolith Production = Erosion + Weathering

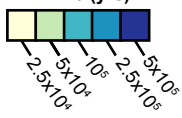


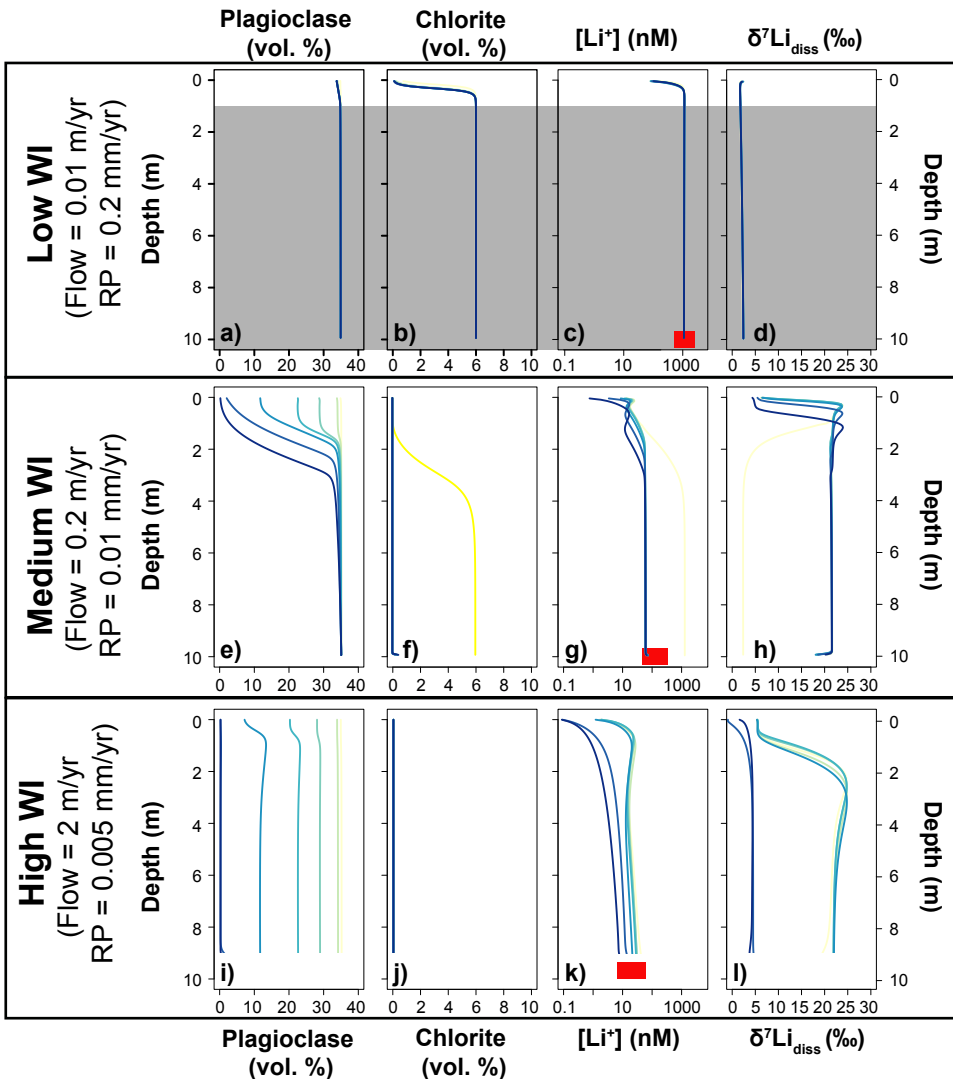




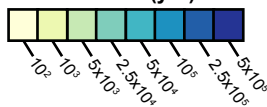


Time (yrs)

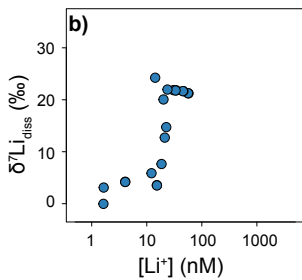
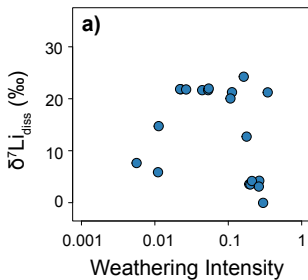




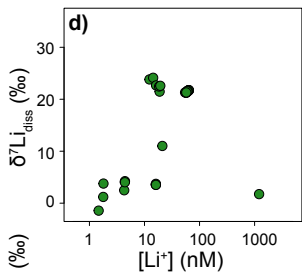
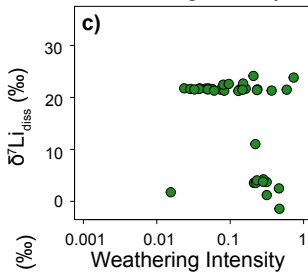
Time (yrs)



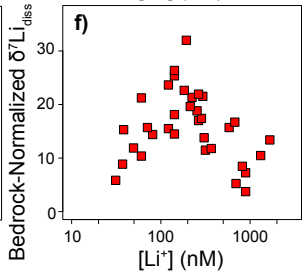
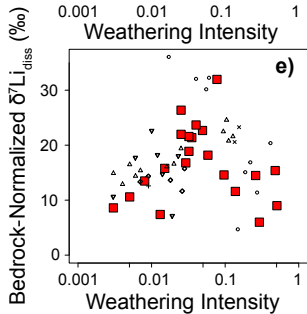
Model
No Chlorite



Model
w/ Chlorite



Data



- Dellinger et al. (2015)
- Huh et al. (2001)
- △ Millot et al. (2010)
- + PVS et al., (2006)
- × PVS et al., (2010)
- ◇ Vigier et al., (2009)
- ▽ Wang et al. (2015)

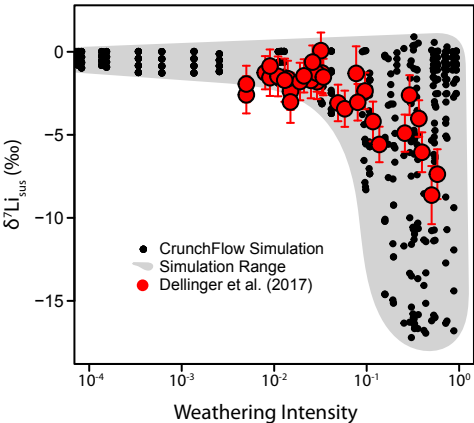


Table A1. CrunchFlow reaction network with 2:1 clay phase.

Mineral	Reaction	log(K _{eq}) @ 298 K	log(k)
Plagioclase (An ₂₀)	$\text{Ca}_{0.2}\text{Na}_{0.79739}{}^7\text{Li}_{0.002409}{}^6\text{Li}_{0.0001948}\text{Al}_{1.2}\text{Si}_{2.8}\text{O}_8 \leftrightarrow 0.2\text{Ca}^{2+} + 0.79739\text{Na}^+ + 0.002409{}^7\text{Li}^+ + 0.0001948{}^6\text{Li}^+$ + 1.2AlO ₂ ⁻ + 2.8SiO ₂ (aq)	-20.076	-14.84
Quartz	SiO ₂ (qz) ↔ SiO ₂ (aq)	-3.9993	-55
Ca-Beidellite_7Li	$\text{Ca}_{0.165-0.5x}{}^7\text{Li}_x\text{Al}_{2.33}\text{Si}_{3.67}\text{O}_{10}(\text{OH})_2 + 7.32\text{H}^+ \leftrightarrow (0.165-0.5x)\text{Ca}^{2+} + 2.33\text{Al}^{3+} + x{}^7\text{Li}^+ + 3.67\text{SiO}_2(\text{aq}) +$ 4.66H ₂ O *	5.59	-17.14
Ca-Beidellite_6Li	$\text{Ca}_{0.165-0.5x}{}^6\text{Li}_x\text{Al}_{2.33}\text{Si}_{3.67}\text{O}_{10}(\text{OH})_2 + 7.32\text{H}^+ \leftrightarrow (0.165-0.5x)\text{Ca}^{2+} + 2.33\text{Al}^{3+} + x{}^6\text{Li}^+ + 3.67\text{SiO}_2(\text{aq}) +$ 4.66H ₂ O *	5.59	Precip: -17.13225 Diss: -17.14

* x varies from 0.000402 - 0.004945

